

$\text{N}_2\text{H}^+(1-0)$ as a tracer of dense gas in and between spiral arms

Orsolya Fehér¹,^{1*} S. E. Ragan¹, F. D. Priestley¹, P. C. Clark¹ and T. J. T. Moore²

¹*School of Physics and Astronomy, Cardiff University, Queen's Buildings, The Parade, Cardiff C24 3AA, UK*

²*Astrophysics Research Institute, Liverpool John Moores University, IC2, Liverpool Science Park, 146 Brownlow Hill, Liverpool L3 5RF, UK*

Accepted 2024 March 27. Received 2024 March 27; in original form 2023 December 7

ABSTRACT

Recent advances in identifying giant molecular filaments in Galactic surveys allow us to study the interstellar material and its dense, potentially star forming phase on scales comparable to resolved extragalactic clouds. Two large filaments detected in the $^{13}\text{CO}/\text{C}^{18}\text{O}(J = 3-2)$ Heterodyne Inner Milky Way Plane Survey (CHIMPS) survey, one in the Sagittarius-arm and one in an interarm region, were mapped with dense gas tracers inside a 0.06 square degrees area and with a spatial resolution of around 0.4 and 0.65 pc at the distance of the targets using the 30 m telescope of the Institut de Radioastronomie Millimétrique (IRAM) to investigate the environmental dependence of the dense gas fraction. The $\text{N}_2\text{H}^+(1-0)$ transition, an excellent tracer of the dense gas, was detected in parsec-scale, elliptical clumps and with a filling factor of around 8.5 per cent in our maps. The N_2H^+ -emitting areas appear to have higher dense gas fraction (e.g. the ratio of N_2H^+ and ^{13}CO emission) in the interarm than in the arm which is opposite to the behaviour found by previous studies, using dust emission rather than N_2H^+ as a tracer of dense gas. However, the arm filament is brighter in ^{13}CO and the infrared emission of dust, and the dense gas fraction determined as above is governed by the ^{13}CO brightness. We caution that measurements regarding the distribution and fraction of dense gas on these scales may be influenced by many scale- and environment-dependent factors, as well as the chemistry and excitation of the particular tracers, then consider several scenarios that can reproduce the observed effect.

Key words: ISM: molecules – ISM: structure – galaxies: star formation.

1 INTRODUCTION

Star formation is an essential element of all aspects and scales of astrophysics from the evolution of galaxies to the birth of planetary systems. The central aim of star formation research is to make a quantitative connection between the physical properties of interstellar gas and the star formation rate (SFR) within. The Kennicutt–Schmidt relation demonstrates that the surface densities of gas and star formation are related when averaged over a galaxy disc (Schmidt 1959; Kennicutt 1998), however, higher angular resolution surveys reveal significant galaxy-to-galaxy variations (Bigiel et al. 2008; Shetty et al. 2014). In nearby molecular clouds of the Milky Way the amount of star formation scales directly with the fraction of gas above a certain density threshold (Lada, Lombardi & Alves 2010), the so-called dense gas mass fraction but whether this diagnostic holds up in all Galactic environments is not well known. Whether a cloud resides in a spiral arm may be a key environmental factor (e.g. Schinnerer et al. 2017), but the current consensus is that the arms themselves do not significantly enhance star formation (Moore et al. 2012; Eden et al. 2013; Ragan et al. 2016).

A major issue in interpreting the Kennicutt–Schmidt relation and its connection to similar Galactic results is insufficient knowledge of our tracers (density, gas temperature, radiation field, opacity, and abundance conditions of their excitation) and the incongruity in their

usage in extragalactic and Galactic investigations. In extragalactic studies, ^{12}CO is often used as a tracer of ‘dense’ star forming molecular gas, while ‘diffuse’ gas is probed by atomic hydrogen. In Galactic studies, CO serves as the ‘diffuse’ tracer and dust or higher critical density molecular-line tracers (e.g. HCN, HCO^+ , N_2H^+) probe the dense gas most closely associated with star formation. Among the possible dense gas tracers in the radio regime, N_2H^+ specifically was shown to be perhaps even better at tracing dense gas than HCN (Forbrich et al. 2014; Shirley 2015a; Kauffmann et al. 2017; Pety et al. 2017; Priestley et al. 2023b). The molecule is linear and in a stable closed shell where all electrons are paired and there is only a weak diamagnetic field generated by rotation. The hyperfine structure (HFS) of the rotational transitions forms due to the interaction between this field and the electric quadrupole moments of the two nitrogens. There are seven HF components grouped in three, and their relative strength can be used to measure optical depth. N_2H^+ is more resistant to freeze-out than CO and an ideal line to trace the velocity structure of interstellar structures. N_2H^+ has been regularly observed in both low- and high-mass Galactic star formation regions and protoplanetary discs (e.g. Turner & Thaddeus 1977; Benson et al. 1994; Qi, Öberg & Wilner 2013; Fernández-López et al. 2014; Yu et al. 2018). Its first extragalactic detection was by Mauersberger & Henkel (1991) and since then it has been observed in a few nearby galaxies like M83 (Harada et al. 2019) and recently towards starburst galaxies as a part of the ALMA Comprehensive High-resolution Extragalactic Molecular Inventory (ALCHEMI) project with the Atacama Large Millimeter/submillimeter Array (ALMA, Martín et al. 2021).

* E-mail: fehero@cardiff.ac.uk

Existing observations of dense gas tracers in nearby galaxies have already given interesting results. A survey of HCN in normal and starburst galaxies by Gao & Solomon (2004) revealed a tight correlation between infrared luminosity (a proxy for SFR) and HCN luminosity (a proxy for dense gas) when averaged over a galaxy, suggesting constant SFR per amount of dense gas. A targeted survey of dense clumps in the Milky Way found the same ratio on parsec scales (Wu et al. 2010). However, another investigation of HCN from 300 dense clumps calculated an order-of-magnitude shortfall in the extrapolated total Galactic emission that would be needed for the Milky Way to satisfy the Gao-relation (Stephens et al. 2016). High-resolution studies of HCN and other dense gas tracers in nearby galaxies suggest that the infrared-luminosity/HCN luminosity relation varies significantly with local environment (Bigiel et al. 2016; Sun et al. 2018). There must be other contributors to the overall HCN-luminosity budget of a galaxy and there might also be an intrinsic scatter from region to region.

Due to the angular resolution limits in studies of nearby galaxies, analogous studies of the Milky Way on parsec-scales can instead reveal the origin of dense gas tracer emission. A growing number of unbiased Galactic plane surveys have enabled us to begin linking small to large scales, thus probe the environmental dependence of the physical conditions of star formation. Ragan et al. (2014) identified the first sample of velocity-coherent giant molecular filaments (GMFs) in the Galactic plane which are Milky Way-analogues of the scales probed in nearby galaxies. GMFs have been subsequently identified throughout the inner Galactic plane (e.g. Zucker, Battersby & Goodman 2015; Abreu-Vicente et al. 2016) and were found both along spiral arms and inside interarm regions. The two kinds of regions show differences in dense gas mass fraction and other properties, but due to limited resolution and sparse sampling of dense gas tracers (Wienen et al. 2012; Shirley et al. 2013) we have a long way to go in acquiring a definitive view on how arm and interarm filaments differ. High-contrast, high-resolution, but lower critical density gas tracer measurements over significant sections of the Galactic plane like the Boston University-Five College Radio Astronomy Observatory Galactic Ring Survey (GRS, Jackson et al. 2006), the CO High-Resolution Survey (COHRS, Dempsey, Thomas & Currie 2013), or CHIMPS (Rigby et al. 2016) will aid in constraining the details of spiral disc models, associate spectral features to star forming sites, and allow for source distances to be calculated, enabling the identification of more extragalactic-analogous structures. Two complexes in Orion (Kauffmann et al. 2017; Pety et al. 2017) and the massive star-forming region W49 (Barnes et al. 2020) have been mapped in dense gas tracer emission as well, however, beside these targeted surveys of extreme star forming areas, sampling the full range of environmental conditions and the ordinary molecular gas that comprises most of the plane should also be held priority.

For this purpose, we used the unbiased, high-angular resolution maps of $^{13}\text{CO}(3-2)$ of the CHIMPS survey probing relatively high critical density material to select segments of large-scale filaments inside and between spiral arms for observations with the IRAM 30m telescope. We targeted dense gas tracers at 3 and 1 mm simultaneously, commonly used both in Galactic and extragalactic studies. In Section 2, we introduce the data set and describe the data reduction methods. From Section 3, we focus on the tracer $\text{N}_2\text{H}^+(1-0)$ and derive the spectral characteristics of the molecular emission for each mapped region. We derive the dense gas tracer-to-CO ratio through dense gas mass fraction-analogous parameters across each region and compare the results between arm and interarm structures. Using dendrogram-based clustering, we define N_2H^+ clusters and

their characteristics, compare N_2H^+ -bright and -faint areas and their dust and ^{13}CO emission to find out more about our tracer and the environments it emits in. We discuss the results in Section 4, comparing them to those of other observed Galactic clouds and the beam-averaged quantities found in nearby galaxies. We summarize our findings in Section 5.

2 DATA REDUCTION AND ANALYSIS METHODS

2.1 The CHIMPS survey

The $^{13}\text{CO}/\text{C}^{18}\text{O}(J = 3-2)$ Heterodyne Inner Milky Way Plane Survey (CHIMPS) was carried out using the Heterodyne Array Receiver Program (HARP) on the 15 m James Clerk Maxwell Telescope in Hawaii, covering approximately 18 square degrees in the region $27:5 \leq l \leq 46:4$ and $|b| \leq 0:5$. HARP is a 16-receptor focal-plane array receiver operating over the frequency range of 325–375 GHz, and the Auto-Correlation Spectral Imaging System backend that was used in conjunction provided 250 MHz bandwidth with 61.0 kHz channel width. The velocity width per channel is 0.055 km s^{-1} and the observations were taken in a position-switching raster (on-the-fly) mode. The angular resolution of the observations is 15 arcsec. For more details on the observations, see Rigby et al. (2016).

The position-velocity diagrams for the two CO isotopologues from the CHIMPS survey integrated over the latitude axis show the spiral arms of the Milky Way clearly visible as continuous streams of emission, and inter-arm regions also appear as relatively emission-free areas separating the arms. The distribution of the gas fits reasonably well with a four-arm model with some deviations. Among these, a significant quantity of emission between the Scutum–Centaurus and Sagittarius arm was seen, more clearly than in previous surveys (e.g. Dame, Hartmann & Thaddeus 2001; Lee et al. 2001) or even in GRS or COHRS. The emission could be explained by a number of physical features: a minor spiral arm, an extension of the Scutum–Centaurus arm itself, a bridging or spur structure (Stark & Lee 2006), or a number of spurs forming coherent structures, extending for several degrees (Rigby et al. 2016).

Specifically in the $36^\circ \leq l \leq 38^\circ$ longitude range of the CHIMPS survey area, two distinct ^{13}CO velocity features were seen: emission associated with the Sagittarius spiral arm around 50 km s^{-1} (approximately at $d = 3 \text{ kpc}$) and emission at 70 km s^{-1} (approximately at $d = 5 \text{ kpc}$) when considering the four-arm model of Taylor & Cordes (1993) updated in Cordes et al. (2004). The segments are over 2 degrees in longitude, roughly equivalent to 175 and 100 pc in filament length, respectively. We selected six subregions along these two filaments, focusing both on areas with strong ^{13}CO emission where dense gas tracers are likely to be excited and at least equal area of low-level emission in order to probe a range of gas conditions in both spiral-arm and interarm regions.

2.2 The IRAM 30 m on-the-fly maps

The observations were performed with the IRAM 30 m telescope under the project IDs 033–17 and E02–22 during 2017 August 8–14 and 2023 February 22. Six subregions were chosen towards the large-scale filamentary structures seen on the CHIMPS maps. The regions, four towards the interarm filament and two towards the Sagittarius arm filament, were mapped with the Eight Mixer Receiver at 1 and 3 mm simultaneously. For the 3 mm observations that appear in this study, the Fast Fourier Transform Spectrometer was connected with

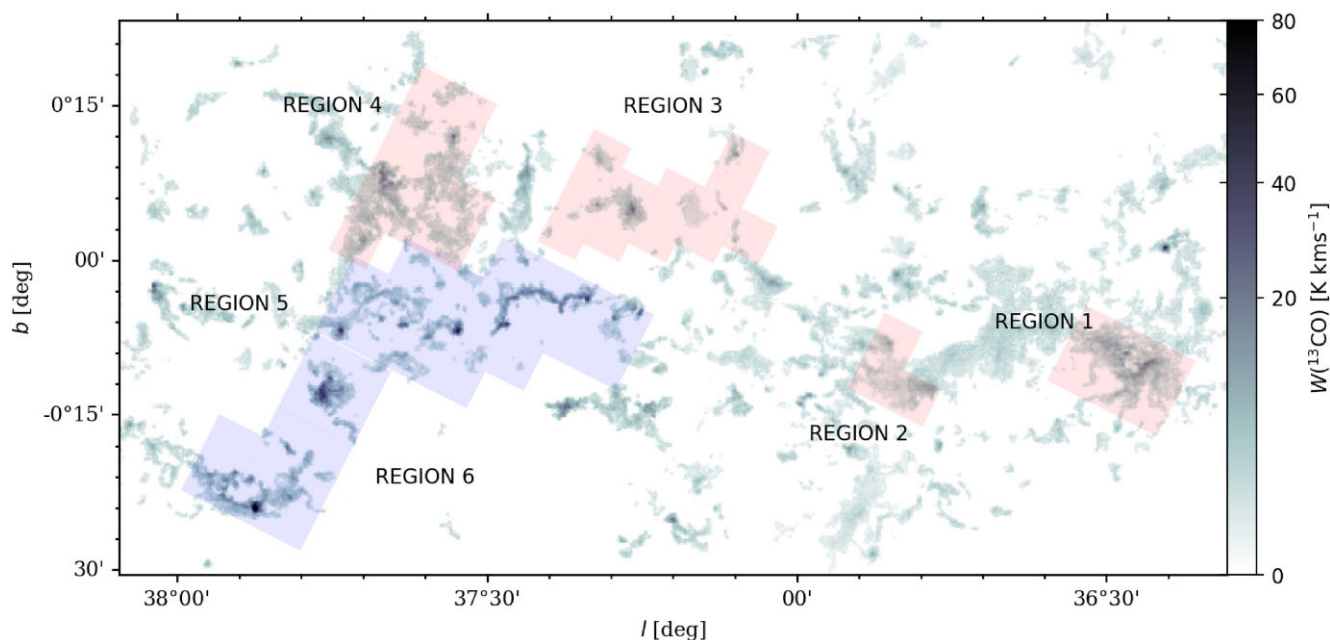


Figure 1. The six selected regions along arm (Region 5 and 6) and interarm filament segments (Regions 1-4) on the CHIMPS $^{13}\text{CO}(3-2)$ integrated intensity maps. The colourmap is normalized with a square-root function to better visually represent the fainter ^{13}CO structures.

the lower sideband tuned to 91.3 GHz, providing 7.7 GHz bandwidth and 200 kHz spectral resolution covering the 85.8–93.4 GHz range, resulting in a velocity resolution of around 0.6 km s^{-1} at the frequency of the $N_2H^+(1-0)$ transition. During project 033–17 we obtained $120 \text{ arcsec} \times 120 \text{ arcsec}$ on-the-fly (OTF) maps with 12 arcsec spacing using position-switching mode, observing 62 of these OTF maps to fill in the chosen filament regions. The half-power beam-width of the telescope at the tuning frequency was 26.9 arcsec. All in all, we spent 44 h on the observations, reaching an average rms noise of 0.1 K (in units of T_A antenna temperature) on each spectral position. Fig. 1 shows the selected regions against the integrated intensity of the CHIMPS $^{13}\text{CO}(3-2)$ observations. All our targeted lines i.e. $\text{HCN}(1-0)$, $\text{HCO}^+(1-0)$, $N_2H^+(1-0)$, $\text{C}^{18}\text{O}(1-0)$ were detected towards both filamentary structures with good signal-to-noise ratio (S/N).

During the reduction and calibration of the data, the presence of negative emission (absorption structures) along the spectral axis made it obvious that the off-positions used in the position-switching observations were not entirely emission-clear. This was expected for CO isotopologues with lower critical densities but not for most dense gas tracers, however, the artifacts could be observed close to the lines in not only HCN and HCO^+ , but even N_2H^+ spectra. To eliminate the effect, we requested time to observe the line emission on the off-positions of the OTF maps. During project E02-22, we performed pointed observations of 54 off-positions from the original measurement set contaminated by emission, using the same tuning setup and position-switching mode. The emission on the off-positions utilized this time were checked with pointed frequency-switched observations first. We reached an observing time of 4.4 min per target position and an average rms noise of 0.02 K (in units of T_A) on each target position. In the end, to correct for the negative features on the OTF maps, we added the emission detected on the off-positions to each target spectra channel by channel. This cleared up the majority of affected positions except a single OTF-map in Region 6 where strong negative emission of unknown origin (not detected when observing the off-position and not likely originating from any known strong radio source in the vicinity) appears on the spectra between

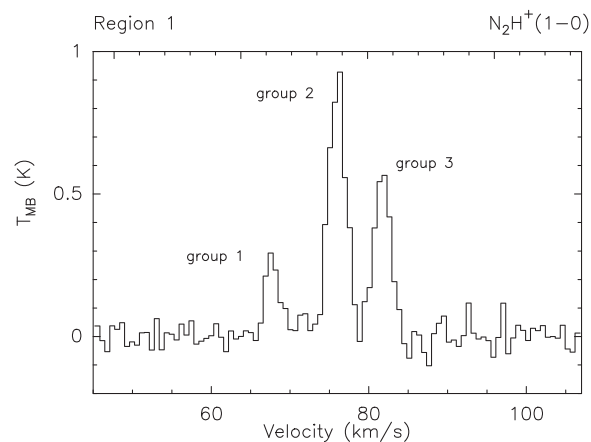


Figure 2. Example spectrum of the detected $N_2H^+(1-0)$ transition in Region 1, averaged in a beam at the position of the integrated intensity maximum. The hyperfine components are seen blended into three lines which are labelled group 1–3.

93.169 and 93.178 GHz. Since this is very close to the science line, the area was excluded from further analysis.

In this paper, we use the observations of the $N_2H^+(1-0)$ transition to trace the densest regions along the arm and interarm filaments. The seven HF components of the $J = 1$ stage of $N_2H^+(1-0)$ were found blended into three groups on our maps (as they generally do under many molecular cloud conditions) and occasionally blended further into a single line with multiple peaks. Fig. 2 presents a typical $N_2H^+(1-0)$ spectrum. The data reduction of the spectra was done with the CLASS and GREG software packages of GILDAS. After baseline subtraction and extraction of the target lines on each spectral position, the OTF maps of a region were brought to the same absolute coordinate system, then the spectral map of the region was regridded using a convolution with a Gaussian and the recommended settings by CLASS to preserve Nyquist-sampling. The resulting cubes have

Table 1. Average spectral parameters from the $\text{N}_2\text{H}^+(1-0)$ emission on the observed regions. (1) Number of region on Fig. 1; (2) Galactic environment seen on CHIMPS maps; (3) number of velocity component; (4) observed line intensities; (5) average v_{LSR} on the region from HFS fitting of $\text{N}_2\text{H}^+(1-0)$ and its standard deviation; (6) average Δv_{HFS} linewidth on the region from HFS fitting and its standard deviation. The averages were calculated on the spectral positions where the peak intensity of the N_2H^+ main group (group 2) was detected with $S/N \geq 3$ (see Section 2.2).

Region	Filament	C	T_{MB} (K)	v_{LSR} (km s^{-1})	Δv_{HFS} (km s^{-1})
1	interarm	1	0.2–1.2	77.8 (6.4)	2.2 (1.8)
		2	0.2–0.6	52.3 (4.4)	1.1 (0.01)
2	interarm	1	0.4–1.2	78.9 (4.5)	1.8 (1.8)
		2	0.4–1.1	53.9 (3.2)	–
3	interarm	1	0.2–3.7	89.9 (4.1)	1.8 (0.8)
4	interarm	1	0.2–2.8	84.6 (3.1)	2.3 (1.8)
		2	0.2–1.2	42.6 (5.2)	1.6 (1.1)
5	arm	1	0.2–2.8	51.1 (6.0)	2.5 (3.5)
6	arm	1	0.2–3.5	65.1 (3.4)	2.7 (1.3)

a pixel size of 5.55 arcsec while the native characteristics of the spectral axis were not changed. The antenna temperatures in the raw data files were converted to T_{MB} main beam brightness temperatures using the ‘modify beam eff /ruze’ command in class which uses the values stored for the 30 m telescope to compute the correction as a function of frequency with Ruze’s equation (Ruze 1966) and rescales the spectra. This correction set the main beam efficiency to 0.81 for all the observed spectra on all channels of the extracted $\text{N}_2\text{H}^+(1-0)$ line.

The integrated intensity, $W(\text{N}_2\text{H}^+) = \int T_{\text{MB}} dv$, of the line was calculated on each pixel by taking the 0th moment of the spectra (see Section 3.1). To derive well-constrained v_{LSR} central velocities and Δv linewidths from the $\text{N}_2\text{H}^+(1-0)$ spectra, we first fitted Gaussian-profiles to the main group (group 2) of the line using the *Gauss* fitting procedure in CLASS on only those pixels where the S/N of $T_{\text{MB},2}$, the main beam brightness temperature of group 2, was higher than 3. The average $\text{N}_2\text{H}^+(1-0)$ spectral parameters detected in the regions are summarized in Table 1. We detect line strengths generally in the interval of 0.2–4 K. The HFS linewidths are between 1 and 3 km s^{-1} with the highest values in Region 6 and the lowest in the lower velocity component of Region 1. We note that due to the generally low S/N spectral data on Region 2, results on this area need to be evaluated cautiously.

Following this, the *hfs* method in CLASS was used to derive τ_{g2} , the optical depth of group 2, $v_{\text{LSR,HFS}}$ HFS central velocity and Δv_{HFS} HFS linewidth with the limit of $S/N \geq 3$ imposed on to the $T_{\text{MB},1}$ main beam brightness temperature of group 1, additionally. On these spectral positions, T_{ex} excitation temperature, τ optical depth, and $N(\text{N}_2\text{H}^+)$ N_2H^+ column density could also be calculated (see Appendix A for the equations).

2.3 Clustering with the dendrogram method

In order to better characterize the structures detected in $\text{N}_2\text{H}^+(1-0)$ emission and to assess the condition of the emitting material, we applied dendrogram clustering to our spectral cubes. There exists a variety of methods for extracting structures from 2D and 3D emission maps of molecular clouds. Dendrograms have the advantage of capturing the hierarchical nature of the interstellar medium, preserving the relationship between the various structures and providing a few easily adjustable parameters to define the depth

of clustering. The analysis begins by locating emission peaks, then grouping the fainter surrounding pixels until two or more local maxima (so-called leaves) contain adjoining pixels. At this point, the two leaves merge at a branch. Fainter pixels are added to the merged structure until it is merged with another or reaches a user-defined noise threshold. At this point, it becomes a trunk. For more detailed discussion of the process, see e.g. Rosolowsky et al. (2008).

Processing a molecular emission cube where HF components are present using dendrogram extraction produces spurious identifications at inaccurate source sizes and central velocities due to the split nature of the lines. To avoid this problem, we followed the example of Keown et al. (2017) and constructed a simulated Gaussian emission data cube based on the emission of the main HF group in our $\text{N}_2\text{H}^+(1-0)$ line emission. Similarly to their process involving $\text{NH}_3(1,1)$ data, a Gaussian spectrum was fitted to the main HF group of the $\text{N}_2\text{H}^+(1-0)$ line on each pixel over the observed maps, scaling the Gaussian functions to the main beam brightness temperature, Gaussian linewidth, and central velocity of the observed group 2 on that position. Then, random noise was added to the Gaussian spectrum with an rms equivalent to the average rms measured in the observed cube. Keown et al. (2017) notes the warning of Friesen et al. (2016) about error being introduced when using this method on spectra containing multiple velocity components. However, our data does not show any sign of close-by multiple velocity components except the two very well-separated components seen towards the arm and interarm filaments, respectively.

We use the ASTRODENDRO package to identify the hierarchical structures in the simulated Gaussian data cubes. The input parameters for the algorithm are: the minimum threshold value to consider in the cube (which we chose as two times the rms noise to be able to pick up fainter structures), the minimum difference in brightness between two structures before they are merged into a branch (which we also set as twice the rms noise) and the minimum number of pixels a structure must contain to remain independent (which we set as three times the pixel-per-beam value in the data set). Using these parameters results in a fairly good selection of N_2H^+ -emitting areas on our maps. However, in some cases, bad pixels on map or spectrum edges were picked up by the process, making later by-eye filtering necessary. We note that especially in the case of Region 2 which has the lowest S/N among the observed spectral cubes, the locations of the identified clusters do not always coincide well with the local peaks on the $\text{N}_2\text{H}^+(1-0)$ integrated intensity map.

We name the derived N_2H^+ clusters as: the letter R signifying ‘region’, followed by the number of the region they appear in, then the letters CL signifying ‘cluster’, followed by a number uniquely identifying the cluster on a certain region in an increasing manner e.g. R1CL1, R1CL2, etc. All in all, 40 N_2H^+ clusters were found by ASTRODENDRO, 16 in the arm and 24 in the interarm filament. None of the extracted clusters show substructure and most of them are small, near-elliptical clumps with major axes generally smaller than 0.5, thus, parsec- and subparsec scale on the sky. They are approximated by the dendrogram extraction process with ellipses.

2.4 Hi-GAL continuum maps and PPMAP

The Herschel Infrared Galactic Plane Survey (Hi-GAL) mapped the inner Milky Way in five infrared bands (70, 160, 250, 350, and 500 μm) to encompass the peak of the spectral energy distribution of cold dust for $8 \leq T_{\text{dust}} \leq 50$ K. In our current study, we made use of the T_{dust} and $N(\text{H}_2)_{\text{dust}}$ maps obtained for the entire Hi-GAL survey range by Marsh et al. (2017) using the point process mapping (PPMAP) procedure (Marsh, Whitworth & Lomax 2015).

The PPMAP tool is a step beyond conventional approaches of calculating column densities in that it does not assume that T_{dust} is uniform in the line of sight. It also enables achieving higher spatial resolutions, since smoothing of the input continuum maps is not required; instead, PPMAP uses the point spread functions of the telescopes directly. Given a set of observational images of dust emission at multiple wavelengths, the associated point-spread functions, a dust opacity law, a grid of temperature values, and assuming that the dust is optically thin, PPMAP performs a non-hierarchical Bayesian process to generate a density function equivalent to a differential column density as a function of angular position and dust temperature.

For the processing of the Hi-GAL data, Marsh et al. (2017) used a power-law form for the dust opacity law:

$$\kappa(\lambda) = 0.1 \text{ cm}^2 \text{ g}^{-1} \left(\frac{\lambda}{300 \mu\text{m}} \right)^\beta \quad (1)$$

with the spectral index $\beta = 2$ based on previous studies. According to Juvela et al. (2012, 2015) the value of β varies between 1.8 and 2.2 in the cold dense interstellar medium, anticorrelates with temperature, and correlates with column density and Galactic position. Using $\beta = 2$ with *Herschel* measurements is appropriate for dense clumps which were expected to be found by the Hi-GAL survey and which are assumed by us to be traced by $N_2H^+(1-0)$ emission as well. The reference opacity $0.1 \text{ cm}^2 \text{ g}^{-1}$ at $300 \mu\text{m}$ is defined with respect to total mass (dust plus gas) and is consistent with a gas to dust ratio of 100 (Hildebrand 1983).

The output of PPMAP with these parameters is first, an image cube of differential column densities with 6 arcsec pixels and 12 arcsec spatial resolution, and 12 values along the temperature axis, covering the range 8–50 K in T_{dust} . The unit of differential column density thus is H_2 molecules per square centimetre per degree Kelvin. The output also includes a corresponding image cube of uncertainties and two more maps: total column density $N(H_2)_{\text{dust}}$ and density-weighted mean dust temperature, T_{dust} . We use these last two maps in this paper. For more information on PPMAP and its use in processing the Hi-GAL data, see further explanations by Marsh et al. (2015, 2017).

A catalogue containing the physical properties of compact sources was also released by Elia et al. (2021) based on the Hi-GAL data set covering the full Galactic plane with more than 150 000 entries, presenting flux density, distance, size, mass, temperature, surface density, luminosity, and classification into evolutionary categories. We use this data to further characterize the gas and the star formation in our target regions.

2.5 Measuring the dense gas fraction

To characterize the volume of gas most likely related to star formation and assess its distribution, environmental dependence, and relation to observable star formation activity tracers, we calculate the dense gas mass fraction-analogous quantities f'_{DG} and $h_{N_2H^+}$.

We define

$$f'_{\text{DG}} = \frac{W(N_2H^+)}{W(^{13}\text{CO})} \quad (2)$$

after the example of Lada et al. (2012) and more recently Bigiel et al. (2016) who examined the variation of dense gas in M51 by showing the trends of the HCN-to-CO ratio across the Galaxy disc and defined $f_{\text{DG}} = M_{\text{dense}}/M_{\text{gas}}$. They use ^{12}CO to trace low-density gas with volume densities of $n \geq 10^2 \text{ cm}^{-3}$ and HCN with the critical density at the order of 10^6 cm^{-3} to trace the dense gas. We note however that Kauffmann et al. (2017) argue that critical densities do

not solely control how line emission couples to dense gas and e.g. HCN already traces characteristic densities at the order of 10^3 cm^{-3} (Jones et al. 2023). In contrast, as discussed before, they regard N_2H^+ as the only molecular species clearly selectively connected to dense gas, a result that is supported by recent theoretical work (Priestley et al. 2023a, b).

The usage of $^{13}\text{CO}(3-2)$ in place of $^{12}\text{CO}(1-0)$ is a similarly complex issue. The optically thin critical density of $^{12}\text{CO}(1-0)$ is 10^3 cm^{-3} at 10 K, however, the transition is almost always strongly optically thick in molecular clouds, so due to radiative trapping, strong lines may be observed in gas with lower than 10^2 cm^{-3} effective critical densities (Shirley 2015b). The isotopologue ^{13}CO generally traces similar densities around 10^3 cm^{-3} , however, its optical depth rarely increases above $\tau = 1-3$. Thus, the radiative trapping effects are not so important and ^{13}CO will generally trace the somewhat denser parts of a molecular structure. Critical density is also not only the function of species but transition, with higher transitions tracing higher densities. The (3–2) transition of ^{13}CO has a critical density of $1.6 \times 10^4 \text{ cm}^{-3}$ as noted by Rigby et al. (2016) based on Schöier et al. (2005) thus it is more sensitive to higher density gas. The amount of detectable emission under the critical density is dependent on the density and the excitation temperature, and we expect to not trace some of the diffuse molecular material on the edges of the clouds using the CHIMPS $^{13}\text{CO}(3-2)$. One advantage however, is that confusion with separate structures at different distances along the line of sight that the (1–0) transition might suffer from is minimized. With these considerations we use the above defined f'_{DG} , the ratio of the integrated intensities of $^{13}\text{CO}(3-2)$ and $N_2H^+(1-0)$, as analogous to the dense gas mass fraction.

The mosaic $^{13}\text{CO}(3-2)$ cube corresponding to our target area on the sky from the CHIMPS survey is available publicly in the Canadian Advanced Network for Astronomical Research (CANFAR) archive.¹ We integrated the $^{13}\text{CO}(3-2)$ emission in the same velocity intervals that we detected $N_2H^+(1-0)$ at and used these respective maps when computing f'_{DG} or comparing the integrated intensities of ^{13}CO and N_2H^+ , to make sure we are comparing radiation emitted from the same volume of material (see Section 3.1). The $N_2H^+(1-0)$ maps with originally 5.5 arcsec pixel size were resampled to the CHIMPS pixel size (7.6 arcsec) for these purposes. To be able to examine tendencies, we calculated f'_{DG} in each beam in our target regions using the beam size of the IRAM telescope (26.9 arcsec) which is larger than the CHIMPS beam (15.2 arcsec).

We can also define

$$h_{N_2H^+} = \frac{W(N_2H^+)}{N(H_2)_{\text{dust}}} \quad (3)$$

following the analysis of Kauffmann et al. (2017) who used the line-to-mass ratio $h_Q = W(Q)/A_V$ in their analysis. Since $A_V \propto N(H_2)$, h_Q essentially measures the intensity of line emission per H_2 molecule. The trend of h_Q versus $N(H_2)$ is non-trivial and differs between molecules. We resampled the $W(N_2H^+)$ maps from their 5.5 arcsec pixels to 6 arcsec which is the Hi-GAL pixel size, to be able to compare the two, and when computing the beam-averaged values of $h_{N_2H^+}$, we used the beam size of the IRAM telescope, 26.9 arcsec since it is larger than the spatial resolution of the PPMAP output $N(H_2)_{\text{dust}}$ map, 12 arcsec.

Both f'_{DG} and $h_{N_2H^+}$ can be thought of as a measure of the dense gas fraction. We emphasize here that most previous studies use the parameter ‘dense gas mass fraction’, usually calculating the masses

¹<http://dx.doi.org/10.11570/16.0001>

of total gas and dense gas inside a structure and comparing the results, while the parameters calculated in this work are not mass fractions, thus we use ‘dense gas fraction’ when talking about f_{DG} and $h_{\text{N}_2\text{H}^+}$.

The used parameters f_{DG} and $h_{\text{N}_2\text{H}^+}$ have their own caveats. CO becomes optically thick then starts depleting at high-volume densities and we also have increasing evidence that a large amount of material exists as CO-dark gas in giant molecular clouds (Wolfire, Hollenbach & McKee 2010; Glover & Mac Low 2011; Smith et al. 2014). Thus ^{13}CO might underestimate the total gas mass in varying degrees in different environments. $N(\text{H}_2)_{\text{dust}}$ calculated from far-infrared or sub-millimeter continuum radiation measures the total amount of material in a column at each line of sight, however, without velocity information, background and foreground clouds not associated with the target object may also contribute to the computed quantity. Biases in determining T_{dust} , using the incorrect dust spectral index, and erroneous assumption of the gas-to-dust ratio can introduce uncertainties in the measure as well. There is also a dependence of the N_2H^+ emission efficiency on T_{dust} as seen by (Barnes et al. 2020) and it shows a differing correlation with CO and HCN emission on different scales (Jiménez-Donaire et al. 2023). In spite of this, recent advances in observing N_2H^+ in varying Galactic and extragalactic environments shed light to its unique chemistry allowing it to trace dense cores (e.g. Kauffmann et al. 2017; Pety et al. 2017). Examining its relation to ^{13}CO is a satisfying measure of the dense gas fraction to first order and gives an excellent opportunity to further investigate the emission of this tracer, filling the scale-gap between its detections in Galactic clouds and in large extragalactic environments.

3 RESULTS

3.1 $\text{N}_2\text{H}^+(1-0)$ in the arm and the interarm

We detected the $\text{N}_2\text{H}^+(1-0)$ transition towards all our target regions. We compute the filling factor as the ratio of pixels on which the main group of the $\text{N}_2\text{H}^+(1-0)$ HFS shows $S/N > 3$ and the total number of pixels. The filling factor is 8.6 per cent on the overall observed area (and 7 per cent, 8 per cent, 15 per cent, 10 per cent, 5 per cent, and 7 per cent in Regions 1–6, respectively). We generally detect the seven HF components of the line blended into three groups as mentioned before, or even blended into a single line with multiple peaks. In lower S/N areas, occasionally the weakest group 1 of the HFS was not detected.

The v_{LSR} values of the detected $\text{N}_2\text{H}^+(1-0)$ lines in the interarm filament regions (Regions 1–4) correspond well with the 60–105 km s^{-1} velocity range defined from the CHIMPS ^{13}CO structure there, but in smaller areas, another, secondary velocity components in the 26–52 and 42–61 km s^{-1} range can also be seen. Some of these were later identified as clusters R1CL7 and R4CL8. Towards Region 5 and 6, the two arm filament sections, the main source of the $\text{N}_2\text{H}^+(1-0)$ emission appears between 31 and 64 km s^{-1} and 50–77 km s^{-1} , respectively. These are the velocities where we expect structures connected to the Sagittarius arm to lie. We only find localized emission at differing velocities on these two regions: weak emission in Region 5 between 6.8 and 32.5 km s^{-1} and in Region 6 between 69 and 94 km s^{-1} . The low-velocity component in Region 5 was excluded from further analysis because it falls outside the velocity region where the two target filaments were defined on the CHIMPS maps. The high-velocity emitting area in Region 6 was excluded because it is close to the edge of the mapped area and the emitting structure likely extends to the area not covered by

observations. Fig. B1 shows the spectra of all the distinct $\text{N}_2\text{H}^+(1-0)$ velocity components observed in our regions.

Figs 3–4 show the $\text{N}_2\text{H}^+(1-0)$ integrated intensity maps for the regions. As limits of the integration, we used the velocity ranges in which the $\text{N}_2\text{H}^+(1-0)$ emission was detected in the different regions. For Region 1–3, the higher velocity components were integrated uniformly between 60 and 105 km s^{-1} while the lower (except Region 3 where there was no lower component found) between 42 and 61 km s^{-1} . For Region 4, the higher velocity component was integrated in the same interval as for the other interarm regions, 60–105 km s^{-1} , however, the lower component was found and integrated between 26 and 52 km s^{-1} . For Region 5 and 6 the integration intervals were 31–64 and 50–77 km s^{-1} . We note that the same velocity masks were used when computing the integrated intensities of the $^{13}\text{CO}(3-2)$ line, since its emission was generally observed in the same velocity ranges as the $\text{N}_2\text{H}^+(1-0)$ line, thus allowing us to look at the same volume of material without losing flux or S/N for either species.

The detected $\text{N}_2\text{H}^+(1-0)$ emission roughly follows the $^{13}\text{CO}(3-2)$ structures on the CHIMPS maps and the far-infrared dust emission on the Hi-GAL maps. However, in some cases, only weak $^{13}\text{CO}(3-2)$ emission is detected on areas with strong $\text{N}_2\text{H}^+(1-0)$ lines e.g. on Region 3 the area identified as cluster R3CL2 or on Region 6 the areas identified as clusters R6CL3 and R6CL4. The opposite can also be observed e.g. the long arc of $^{13}\text{CO}(3-2)$ emission on Region 5 shows very weak $\text{N}_2\text{H}^+(1-0)$ lines. When looking at the integrated intensity maps of the secondary velocity components, there is generally little correlation between $W(\text{N}_2\text{H}^+)$ and dust structures e.g. the lower velocity component map of Region 4 in Fig. 3.

We derived the beam-averaged values of f'_{DG} and $h_{\text{N}_2\text{H}^+}$ in each region using each pixel where the detected $\text{N}_2\text{H}^+(1-0)$ emission was above zero. Fig. 5(a) shows the distribution of these values for every region. The average values of f'_{DG} are systematically higher for Region 2, 3, and 4 (0.50 ± 0.07 , 0.47 ± 0.06 , 0.33 ± 0.03 , respectively) than for Region 1 and the two arm filament regions, 5 and 6 (with an average of 0.17 ± 0.02 , 0.18 ± 0.02 , 0.19 ± 0.03 , respectively). This is also the case when looking at the averages of $h_{\text{N}_2\text{H}^+}$, and the difference also exists when considering the medians of both parameters.

The regions in the arm filament show higher average $W(^{13}\text{CO})$ and $N(\text{H}_2)_{\text{dust}}$ than the interarm filament (see Fig. 5b), while such difference is less apparent in the $\text{N}_2\text{H}^+(1-0)$ emission which is similarly bright in the two filaments. A correlation between the average $W(^{13}\text{CO})$ of a region and its average f'_{DG} by eye shows that the regions with fainter $^{13}\text{CO}(3-2)$ emission have higher f'_{DG} and the arm filament regions with brighter ^{13}CO emission (along with Region 1) exhibit a lower f'_{DG} . This is also true when looking at f'_{DG} and $h_{\text{N}_2\text{H}^+}$ versus $N(\text{H}_2)_{\text{dust}}$: the denser, CO-brighter arm filament shows a lower dense gas fraction. We quantify these correlations by calculating the Spearman rank-order correlation coefficient between the variables which assesses how well the relation between the variables can be described with a monotonous function. We find Spearman coefficients for the average $W(^{13}\text{CO})$, $W(\text{N}_2\text{H}^+)$, and $W(\text{NH}_2)_{\text{dust}}$ versus average f'_{DG} of 0.83 (p -value: 0.04), 0.66 (0.16), and -0.54 (0.27), respectively. The same assessment for the average $W(^{13}\text{CO})$, $W(\text{N}_2\text{H}^+)$ and $N(\text{H}_2)_{\text{dust}}$ versus average $h_{\text{N}_2\text{H}^+}$ gives -0.60 (0.21), 0.89 (0.02), and -0.60 (0.21), respectively. Only the correlation between the average ^{13}CO brightness and f'_{DG} , and between $W(\text{N}_2\text{H}^+)$ and $h_{\text{N}_2\text{H}^+}$ seem significant, although all coefficients are above 0.5.

Fig. 6 shows the correlations of the beam-averaged integrated intensities of $\text{N}_2\text{H}^+(1-0)$ and $^{13}\text{CO}(3-2)$, alongside the Hi-GAL

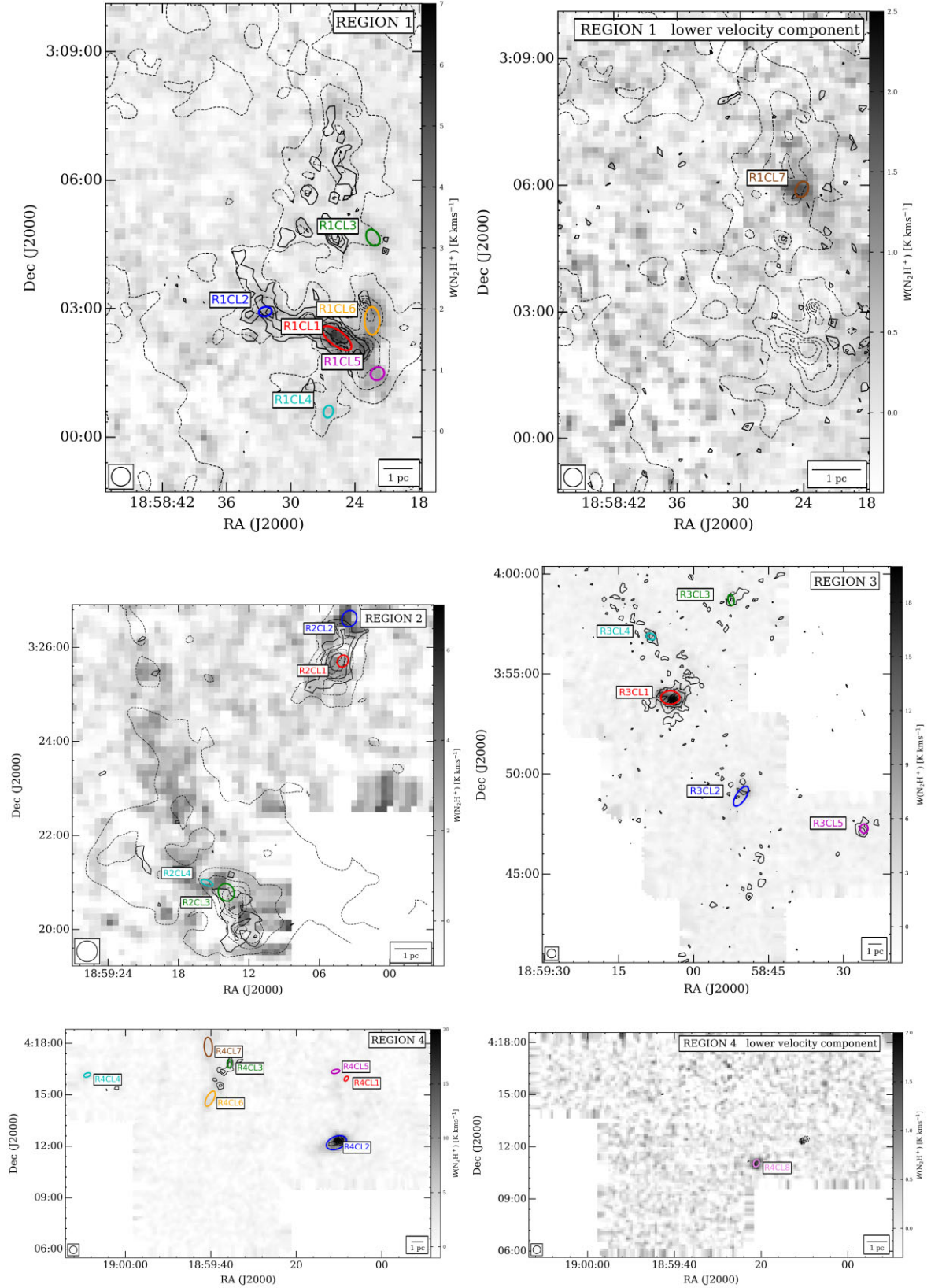


Figure 3. Integrated intensity map of $N_2H^+(1-0)$ for the four regions in the interarm filament, along with their lower velocity line component (for the integration limits see Section 3.1). Continuous contours mark the integrated intensity of $^{13}CO(3-2)$ for the same velocity intervals where contour levels are at 40 per cent, 60 per cent, and 80 per cent of the maxima of the maps [20 (10.2 on the lower velocity map), 16.9, 25.7, and 33.2 (20.8 on the lower velocity map) $K km s^{-1}$, respectively]. Dashed contours mark $N(H_2)_{dust}$ where contour levels are at 20 per cent, 30 per cent...80 per cent of the maximum ($3.1, 2.7, 18.5,$ and $26.0 \times 10^{22} cm^{-2}$, respectively). The ellipses mark the N_2H^+ clusters extracted with the dendrogram clustering.

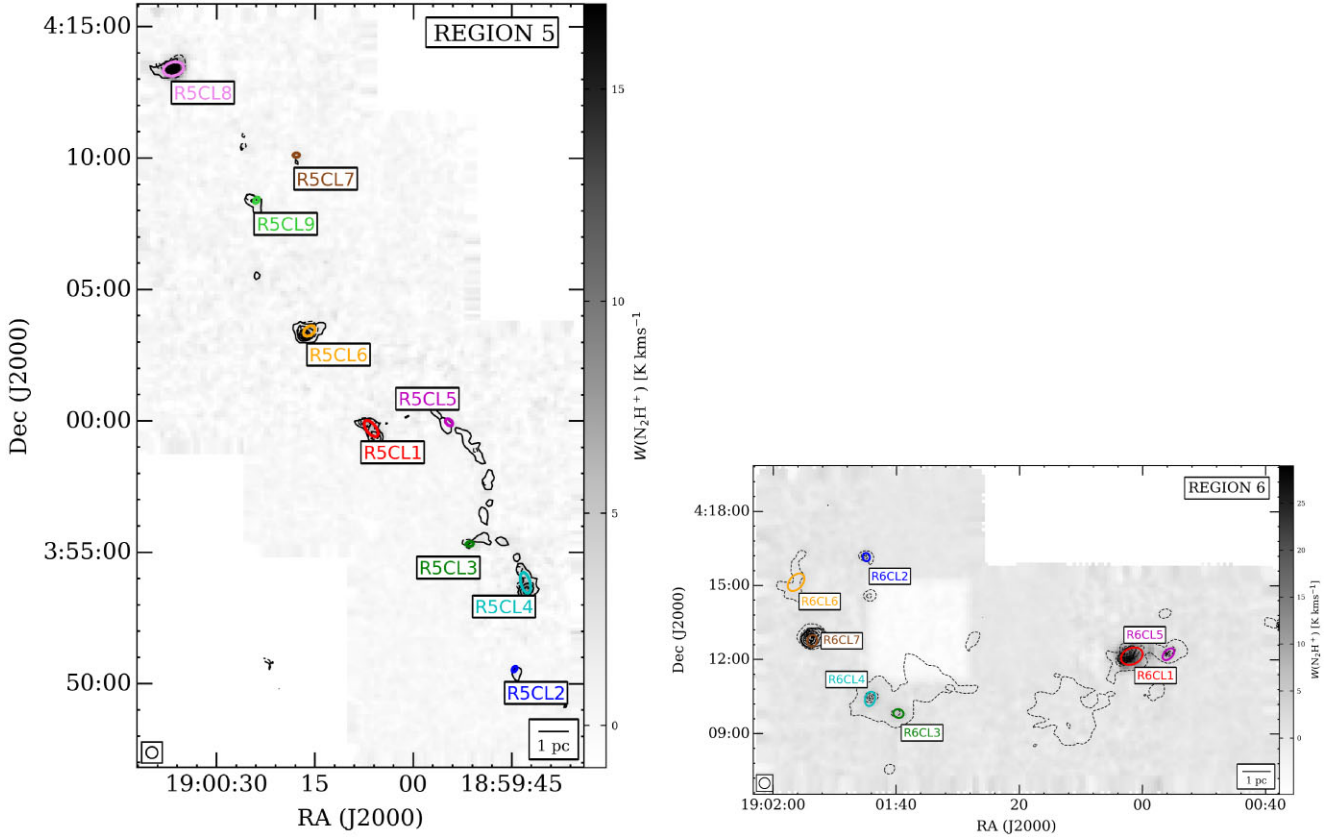


Figure 4. Integrated intensity map of $N_2H^+(1-0)$ for the two regions in the interarm filament (for the integration limits see Section 3.1). Continuous contours mark the integrated intensity of $^{13}CO(3-2)$ for the same velocity intervals where contour levels are at 40 per cent, 60 per cent, 80 per cent of the maxima of the maps (70.9 and 112.0 $K km s^{-1}$, respectively). Dashed contours mark $N(H_2)_{dust}$ where contour levels are at 10 per cent, 20 per cent...80 per cent of the maximum (25.6 and $19.6 \times 10^{22} cm^{-2}$, respectively). The ellipses mark the N_2H^+ clusters extracted with the dendrogram clustering.

based $N(H_2)_{dust}$ for each region. Above the noise level of the $W(N_2H^+)$ maps the integrated intensity of $N_2H^+(1-0)$ generally increases with both increasing $W(^{13}CO)$ and $N(H_2)_{dust}$. The Spearman coefficients between $W(^{13}CO)$ and $W(N_2H^+)$ in Region 1–6 are 0.54, 0.22, 0.27, 0.28, 0.36, and 0.32 (with p -values < 0.01), and between $N(H_2)_{dust}$ and $W(N_2H^+)$ are 0.44, 0.32, 0.23, 0.12, 0.26, and 0.28 (with p -values < 0.01). The data of Region 1 shows the highest coefficient.

3.2 The parsec-scale clustering of $N_2H^+(1-0)$ emission

Fig. 6 also shows that the identified N_2H^+ clusters all appear above certain $W(N_2H^+)$, $W(^{13}CO)$, and $N(H_2)_{dust}$ thresholds. The $W(^{13}CO)$ threshold seems to be larger for Regions 5–6 than for the interarm filament regions, around $8 K km s^{-1}$ instead of $2-5 K km s^{-1}$. The $N(H_2)_{dust}$ threshold for the arm filament regions is also higher, $2 \times 10^{22} cm^{-2}$, while it is around $1.2 \times 10^{22} cm^{-2}$ for Regions 1–4.

The values of f'_{DG} and $h_{N_2H^+}$ computed for the N_2H^+ clusters give $f'_{DG} = 0.46, 0.44, 0.68,$ and 0.80 on average for the clusters in Regions 1–4 and 0.22 and 0.39 for Regions 5–6, thus, an average of 0.60 for the interarm filament and 0.31 for the arm filament (we did not consider R1CL7 and R4CL8 in this computation). This agrees well with the results gained from the beam-averaged values before. The average $h_{N_2H^+}$ values are $1.52, 1.93, 2.60,$ and $2.0 K km s^{-1}/10^{22} cm^{-2}$ for Regions 1–4 (an average

of $2.0 K km s^{-1}/10^{22} cm^{-2}$) and 1.43 and 1.40 for Regions 5–6. Both the average f'_{DG} and the $h_{N_2H^+}$ values of all beams and the averages of the N_2H^+ clusters in the two filaments suggest higher dense gas fraction in the interarm than in the arm. Table B1 contains all the parameters (extent, average spectral parameters, integrated intensities, and column densities) for our identified N_2H^+ clusters.

We associate the clumps from the Hi-GAL catalogue by Elia et al. (2021) to our N_2H^+ clusters to investigate their physical properties further. Out of our 40 N_2H^+ clusters 32 have associated objects in the Hi-GAL sample, 17 in the interarm filament and 15 in the arm filament. The catalogue lists the classification of the clumps based on the existence of $70 \mu m$ Herschel-emission and establishes three groups: protostellar, pre-stellar (starless but bound), and starless (starless and unbound). In the interarm filament, 11 of the N_2H^+ clusters that could be associated with Hi-GAL clumps are protostellar (65 per cent), five are pre-stellar and one is starless (35 per cent). In the arm filament, all 15 associated clumps are protostellar. For comparison, the total number of Hi-GAL clumps in the N_2H^+ -mapped area of the arm filament is 112, from which 21.5 per cent are starless/pre-stellar and 78.5 per cent are protostellar, and in the interarm filament it is 150, from which 53 per cent are starless/pre-stellar, 47 per cent are protostellar.

Fig. 7 shows the correlations of the average $W(N_2H^+)$ versus average $W(^{13}CO)$ and $N(H_2)_{dust}$ for all the interarm and arm filament N_2H^+ clusters. Interarm clusters appear at lower $W(^{13}CO)$ values than arm clusters and their maximum ^{13}CO brightness is also lower.

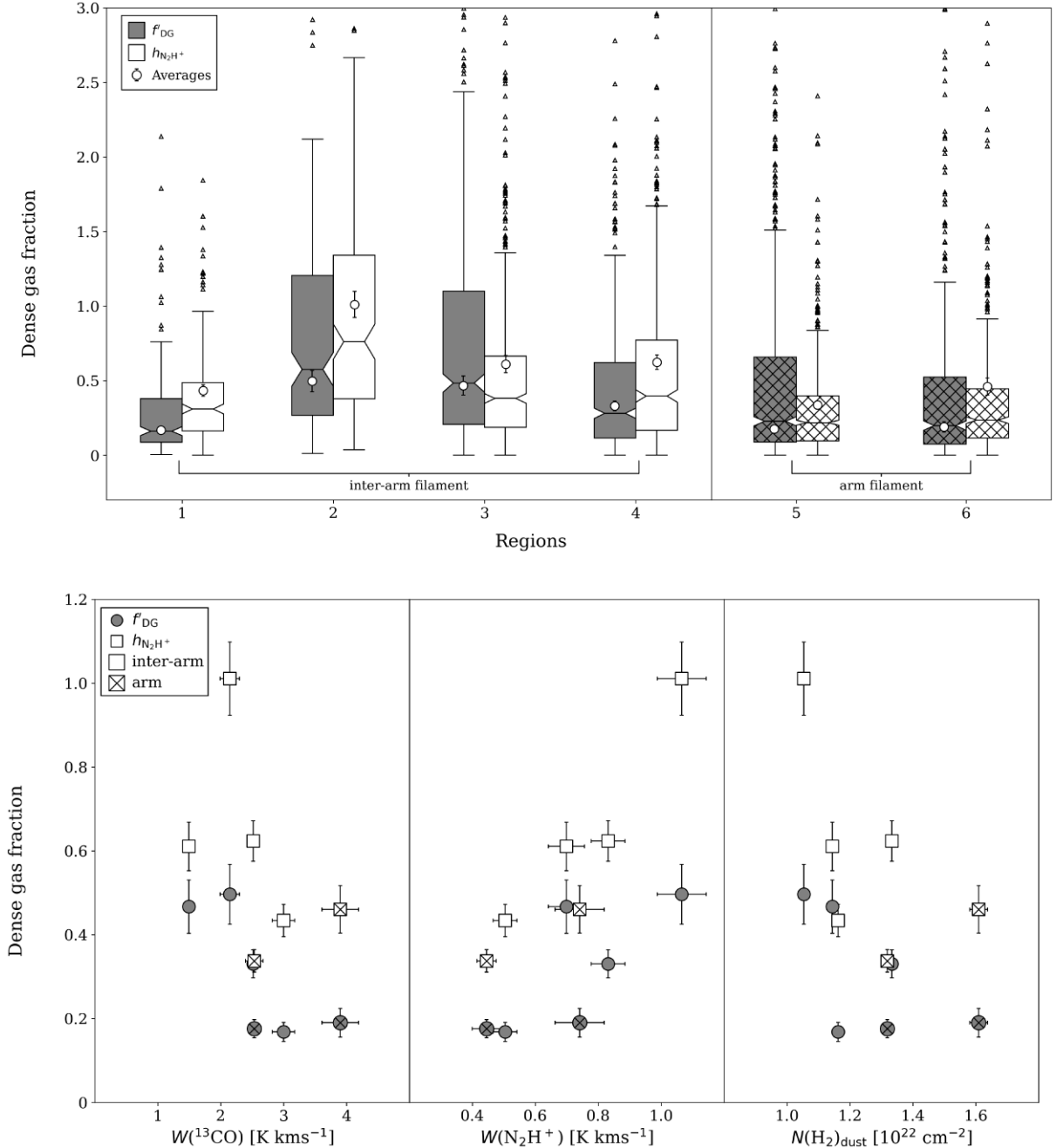


Figure 5. (a) The distribution of the beam-averaged f'_{DG} and $h_{N_2H^+}$ values (the latter in units of $K \text{ km s}^{-1}/10^{22} \text{ cm}^{-2}$) in the six regions. The boxes extend from the first quartile to the third quartile of the data, the notch indicates the confidence interval around the median (horizontal line), the whiskers extend to the farthest data point lying within $1.5 \times$ the interquartile range, and outlier points are indicated with triangles. The first, darker box marks the distribution of f'_{DG} , the second, lighter box the distribution of $h_{N_2H^+}$. Circle symbol marks the average values. Hashed boxes indicate the arm filament regions while non-hashed boxes the interarm filament regions. (b) The average f'_{DG} and $h_{N_2H^+}$ values in each region (the latter in units of $K \text{ km s}^{-1}/10^{22} \text{ cm}^{-2}$) versus the average $^{13}CO(3-2)$ and $N_2H^+(1-0)$ integrated intensities and the $N(H_2)_{dust}$ of a region. The errors are computed as the error of the mean value in every case.

Interarm clusters have roughly constant average $W(N_2H^+)$ at low $N(H_2)_{dust}$ but with increasing column densities, a couple of clusters appear at higher $W(N_2H^+)$ as well. In contrast, arm filament clusters show generally higher $N(H_2)_{dust}$ values and their average $W(N_2H^+)$ starts rising already at $2 \times 10^{22} \text{ cm}^{-2}$. The behaviour of $h_{N_2H^+}$ versus $N(H_2)_{dust}$ differs from that of f'_{DG} versus $W(^{13}CO)$: while the latter shows a general decreasing tendency with $^{13}CO(3-3)$ brightness, the former is mostly constant with increasing $N(H_2)_{dust}$.

Arm clusters are all protostellar where association was possible, and on average, they show bright ^{13}CO emission, high $N(H_2)_{dust}$, and generally low f'_{DG} and $h_{N_2H^+}$. In the interarm, there is no significant difference between the ^{13}CO emission of protostellar or starless/pre-stellar clumps, however the $N(H_2)_{dust}$ of starless/pre-stellar clumps tends to be lower than for the protostellar ones, and only protostellar clumps reach really high N_2H^+ brightness.

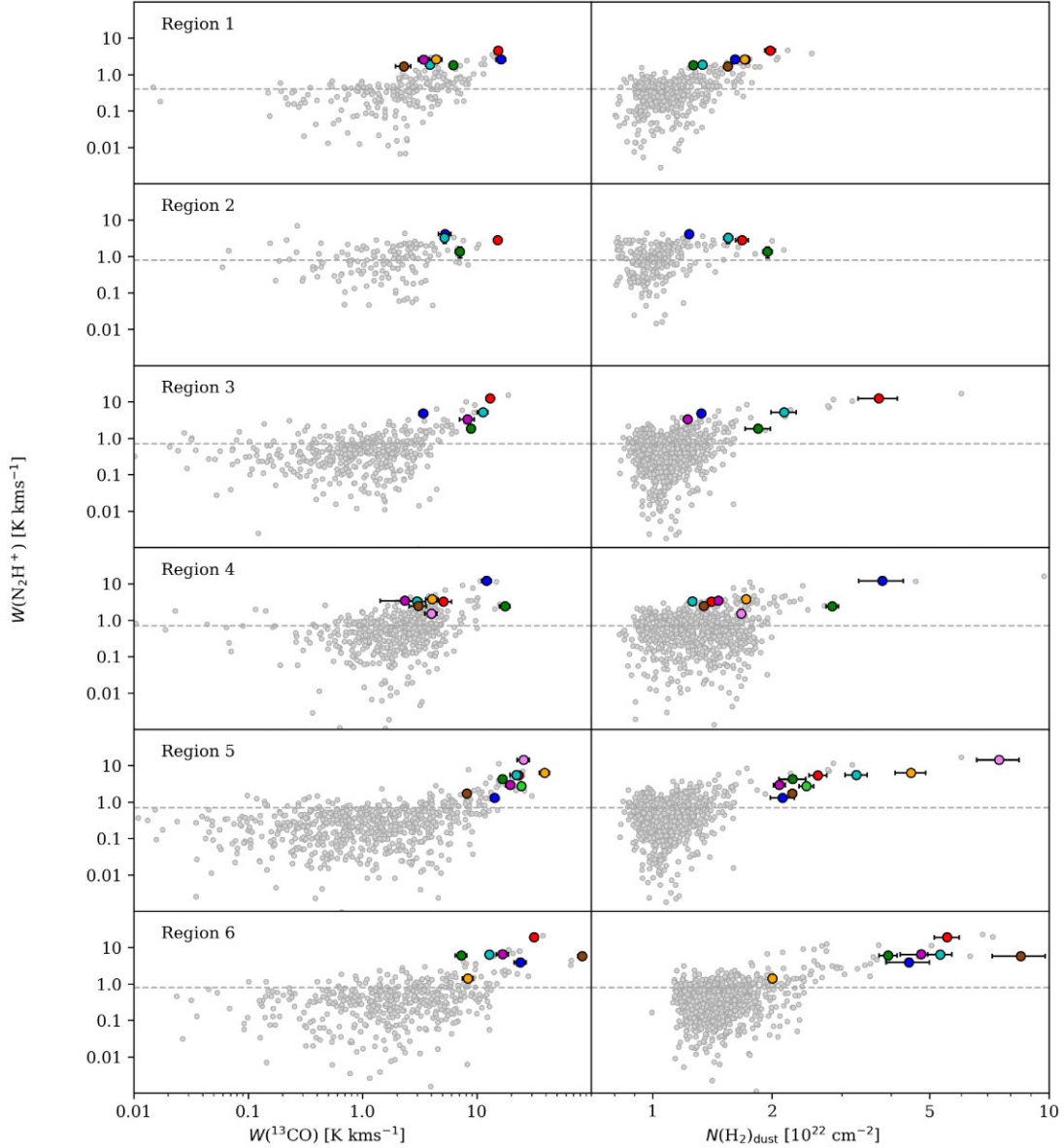


Figure 6. Comparison of the beam-averaged integrated intensities (grey circles) of $^{13}\text{CO}(3-2)$, $\text{N}_2\text{H}^+(1-0)$, and the Hi-GAL-based column density of H_2 on each observed region. The average values of the N_2H^+ clusters are plotted with colours corresponding to the ellipses on Figs 3 and 4. Dotted horizontal lines mark the noise level of the $W(\text{N}_2\text{H}^+)$ maps measured as the rms noise in an emission-free area.

4 DISCUSSION

4.1 The observed scales in context

To better interpret our results, it is advantageous to put the spatial scales of our observations in perspective. The study of Ophiuchus also using the IRAM 30m telescope by André et al. (2007) provides a good opportunity for comparison. They carried out a mapping of $\text{N}_2\text{H}^+(1-0)$ towards the protostellar condensations in the main Ophiuchus molecular cloud to examine the kinematics of the region. Their Fig. 7 shows the large-scale view of their studied cloud containing 41 condensations. The entire region is roughly 1 pc in diameter and thus would fit into one of our N_2H^+ clusters, for example R1CL1, R3CL1, or R4CL2 in the interarm filament or R5CL8 and R6CL6 in the arm filament (the brightest and largest clusters). A comparison of these spectra can be seen in Fig. 8. The $\text{N}_2\text{H}^+(1-0)$ lines appear with

comparable intensities and linewidths to our measurement set, with Ophiuchus showing $\Delta v_{\text{HFS}} = 1.0 \text{ km s}^{-1}$, the shown interarm clusters $1.8\text{--}2.5 \text{ km s}^{-1}$ and the shown arm clusters $3.0\text{--}3.7 \text{ km s}^{-1}$. While the variation in velocity dispersion between the different regions may originate from both intrinsic structure and from integrating many different cloud structures into the beam, the similarity suggests that there is a good chance our N_2H^+ clusters are star forming clouds similar to Ophiuchus, at a larger distance and all their line emission integrated into 1–2 beams.

4.2 Line emission and the dense gas fraction in large-scale Galactic structures

Different samples of GMFs similar to ours but identified by various other methods such as by Ragan et al. (2014), Abreu-Vicente et al. (2016), Zucker et al. (2015), and Wang et al. (2015, 2016), were found

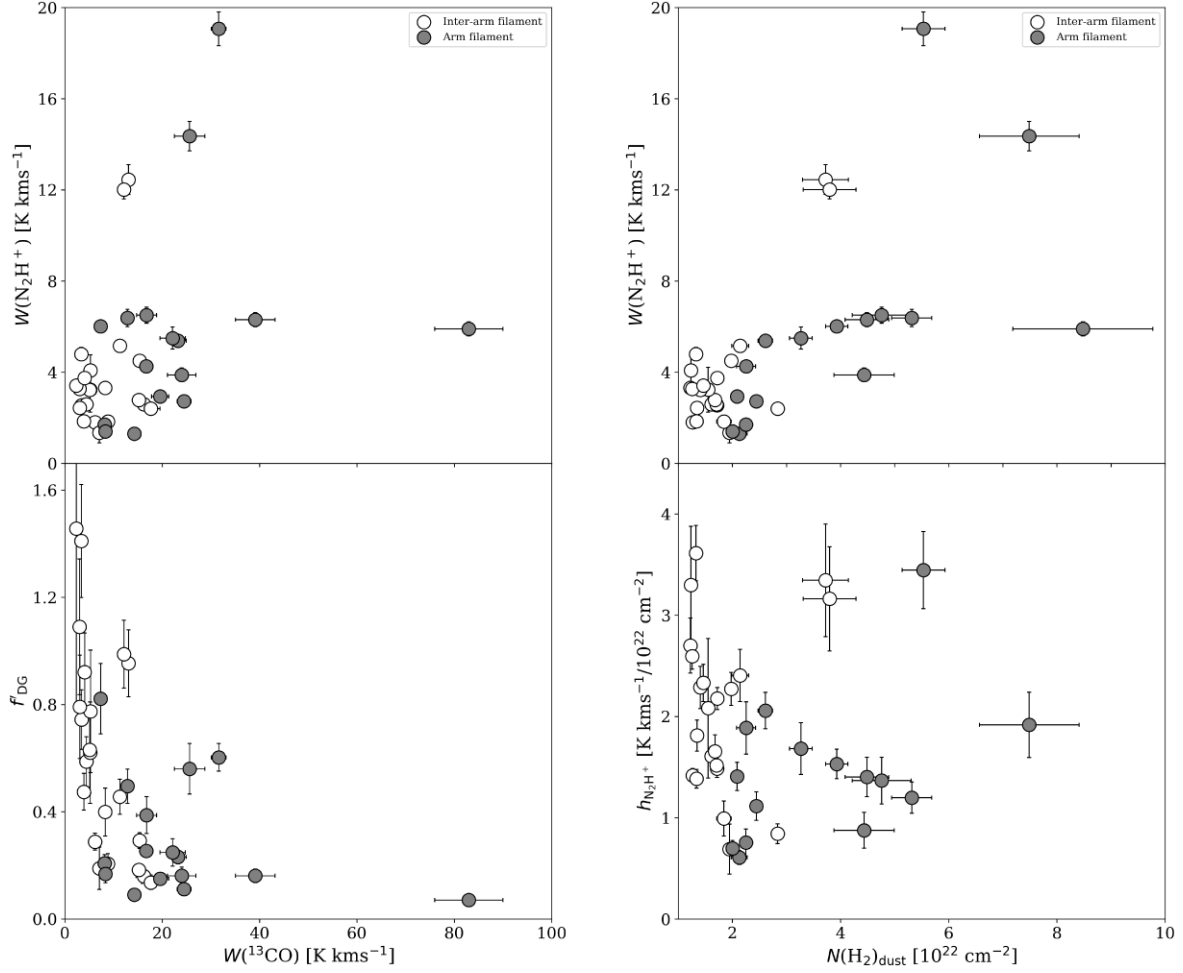


Figure 7. The correlation of the average $N_2H^+(1-0)$ integrated intensity, $^{13}CO(3-2)$ integrated intensity, H_2 column density, and the two types of dense gas fraction measures in the N_2H^+ clusters of the arm and interarm filaments.

to vary in their physical parameters (aspect ratio, linear mass and column density) signifying true differences in their physical states, and potentially origin and role in the Galactic structure Zucker et al. (2018). The filaments studied by us have full lengths at the middle of the range they investigated (11–269 pc) and are more similar to their so-called elongated giant molecular cloud specimens.

The dense gas mass fraction for these samples of filaments were calculated in various ways. For the GMFs in the sample of Ragan et al. (2014), the dense gas mass fraction was determined from the ratio of dense gas mass measured by the APEX Telescope Large Area Survey of the Galaxy (ATLASGAL) $870\mu\text{m}$ maps divided by the total gas mass measured by the GRS ^{13}CO survey. They found a dense gas mass fraction of 1.6–12 per cent for their interarm objects which is consistent with values for other large molecular filaments, local star-forming clouds, high-mass regions, and local star-forming clumps (Johnston et al. 2009; Kainulainen et al. 2009; Lada et al. 2010; Lada et al. 2012; Kainulainen et al. 2013; Battersby & Bally 2014; Battisti & Heyer 2014). They also found that the dense gas mass fraction decreases with increasing galactocentric radius, increases towards the mid-plane, and the GMF closest to a spiral arm shows the highest value. The work by Abreu-Vicente et al. (2016) calculates the dense gas mass fraction the same way and finds values between 1.5 per cent and 14 per cent with one filament related to a massive HII complex showing 37 per cent. They see no correlation with

distance from the mid-plane. In their sample, arm filaments also show higher dense gas mass fraction, although most of their objects are in the arm. In contrast with this, we find higher values of f'_{DG} for our interarm filament than for the Sagittarius-arm filament, both when looking at general trends and in the extracted N_2H^+ clusters (with the caveat that our method of deriving dense gas fraction is different than in the studies mentioned above). We note that the first GMF identified, ‘Nessie’, a structure inside a spiral arm, shows around 50 per cent dense gas mass fraction, derived from HNC (1–0) emission tracing the dense gas (Jackson et al. 2006; Goodman et al. 2014).

The brightness of $^{13}CO(3-2)$ and dust emission shows differences between our two filaments with the arm filament generally showing higher values, while the $N_2H^+(1-0)$ brightness is generally similar in the two environments. Moore et al. (2012) examined cloud masses and young stellar object (YSO) content in the GRS survey region and concluded that most of the observed increase in star-formation rate density associated with spiral arms is due to source crowding and there is little or no increase in star-formation efficiency (SFE) on kiloparsec scales. Eden et al. (2013) studied the GRS clouds by associating dense clumps to them from the Bolocam Galactic Plane Survey (Aguirre et al. 2011) sample and found no evidence of difference in clump-formation efficiency (CFE, which can be thought of as a precursor-analogue of SFE) between interarm and spiral-

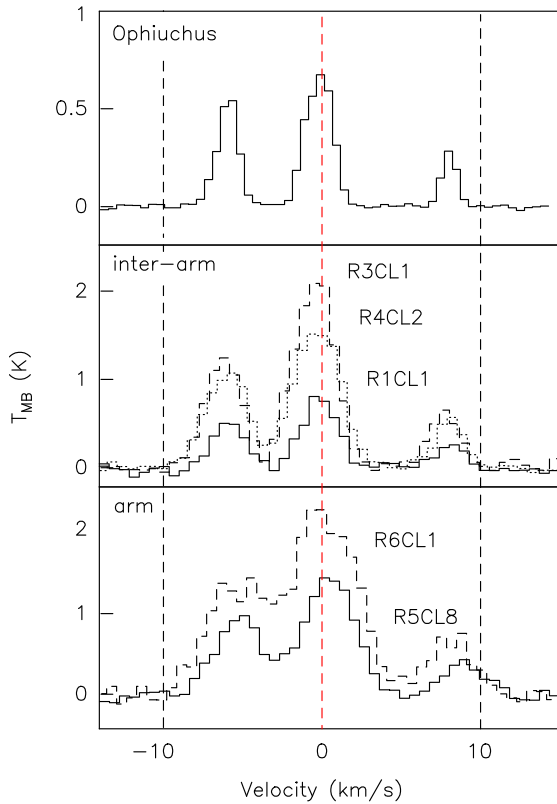


Figure 8. The average $N_2H^+(1-0)$ spectrum of the Ophiuchus main cloud based on the observations of André et al. (2007) and the average spectra of three interarm and two arm filament clusters. All spectra were centred to $v_{LSR} = 0$ for simple comparison purposes. The spectrum of Ophiuchus was also smoothed to be presented with a similar velocity resolution (0.5 km s^{-1}) as the other spectra (0.63 km s^{-1}).

arm regions. Schinnerer et al. (2017) performed a multiwavelength study of a spiral arm segment in M51 and found no variation in giant molecular cloud (GMC) parameters between arm and interarm clouds, and no evidence of a coherent star formation (SF) onset mechanism that can be solely associated with the arms. In contrast, in our sample, both ^{13}CO and dust infrared (IR) emission average and maximum brightness show differences between interarm and arm regions. It looks like there is more dense gas to form stars in the interarm than in the spiral-arm cloud but since the $N_2H^+(1-0)$ emission does not show significant differences in strength between the two environments, the derived dense gas fraction values and their tendencies are controlled by our method of measuring the total gas, thus the ^{13}CO integrated intensities and the H_2 column densities. Measuring total gas with ^{13}CO , the derived f'_{DG} values show large differences in the two filaments and also a decreasing tendency versus ^{13}CO brightness (see Fig. 7). These differences and tendencies diminish when deriving total gas using the IR continuum, thus H_2 column densities. We also find only protostellar Hi-GAL clumps on our mapped area in the arm filament, while the ratio of protostellar objects in the interarm is much lower.

The Hi-GAL-based dust temperatures on the maps derived by PPMAP do not seem to be very different for the two filaments, however some difference can be seen in the average temperatures of the Hi-GAL clumps computed by Elia et al. (2021) where the clumps in the arm are warmer. The average $^{13}\text{CO}(3-2)$ brightness inside arm filament sources also shows a positive correlation with the temperatures of the clumps, while the $N_2H^+(1-0)$ brightness does

not. The $^{13}\text{CO}(3-2)$ brightness– T_{dust} correlation does not apply in the interarm filament.

4.3 How do we measure the dense gas fraction?

Pety et al. (2017) concludes in their investigation of Orion B that despite the similar critical densities of N_2H^+ and HCO^+ , their emitting behaviour is different. In their data set, N_2H^+ is only emitting from dense regions while HCO^+ is not. N_2H^+ only survives in regions where the electron abundance is low (which prevents dissociative recombination) and where CO is frozen on to dust grains (which prevents proton transfer to CO). Thus, they propose to use $N_2H^+ / ^{12}\text{CO}$ as a dense gas fraction measure. They measure the flux ratios of species e.g. $^{12}\text{CO}/N_2H^+$ which is 900 in Orion B. Collected values from the literature are: 40 in ultra-luminous infrared galaxies and 59–167 for the Large Magellanic Cloud (Nishimura et al. 2016), 225 for M51 P2 (Watanabe et al. 2014), 41–68 for active galactic nuclei (AGNs), and 100–325 for starburst galaxies (Aladro et al. 2015). The value of $^{13}\text{CO}/N_2H^+$ in our N_2H^+ clusters is generally around 1–5 which should result in a $^{12}\text{CO}/N_2H^+$ of 50–250 working with a $^{12}\text{CO} = 45\text{--}55 \times ^{13}\text{CO}$ from $^{12}\text{CO}/^{13}\text{CO} = 5.41R_{\text{gal}} + 19.3$ at $R_{\text{gal}} \approx 5\text{--}7$ by Milam et al. (2005). However, since ^{12}CO is usually optically thick, affecting the measured line intensity, towards real star forming sites the $^{12}\text{CO}/^{13}\text{CO}$ ratio is closer to 10 (Tafalla, Usero & Hacar 2023). The conversion is also dependent on the specific transitions used. $^{13}\text{CO}(3-2)/^{13}\text{CO}(1-0)$ is probably lower than 1, increasing $^{12}\text{CO}/N_2H^+$, thus making this comparison riddled with uncertainties. Pety et al. (2017) measures a filling factor of 2.4 per cent and an abundance of 2×10^{-11} – 3×10^{-9} for N_2H^+ in Orion B versus our 8.6 per cent and 1.5×10^{-10} – 1.06×10^{-9} .

Kauffmann et al. (2017) investigated Orion A for the Molecular Line Emission as a Tool for Galaxy Observations (LEGO) project using several molecular species (e.g. CO isotopologues, CN, CCH, HCN, N_2H^+). They measured the behaviour of $h_Q = W(Q)/A_V$ versus A_V for the molecules and saw a trend for CO isotopologues, C_2H , HCN, and CN where h_Q is high at low A_V , the value increases to a maximum around 5–20 mag of A_V then steadily decreases. In contrast, the h_Q values for N_2H^+ begin at nearly zero at low A_V then start rising around 10 mag to reach a maximum or a plateau around 100 mag. We measure A_V around 10–16 in our current study and see a roughly constant behaviour of $h_{N_2H^+}$ versus $N(\text{H}_2)_{\text{dust}}$ (with scatter) as predicted by Priestley et al. (2023b).

Barnes et al. (2020) presented a map of the massive star forming region W49 ($d \approx 11 \text{ kpc}$) with the IRAM 30 m telescope in the emission of several molecular species for the LEGO project. They also use the h_Q measure after Kauffmann et al. (2017). Their Fig. 7 shows an increase of $W(N_2H^+)$ versus $N(\text{H}_2)_{\text{dust}}$ starting slightly below 10^{22} cm^{-2} from a plateau that appears on our figures for our targeted filament regions as well (Fig. 6). In their sample the CS, CH_3OH , HCO^+ , and N_2H^+ integrated intensities rise the quickest with increasing $N(\text{H}_2)_{\text{dust}}$. Their values of h_Q show a quick rise with $N(\text{H}_2)_{\text{dust}}$ and a turnoff point around $5 \times 10^{22} \text{ cm}^{-2}$ (similarly to e.g. HCO^+ , CN, CS, HCN, HNC) and they found that their results regarding h_Q are in good agreement with Pety et al. (2017). This was a surprising conclusion because of the very different resolution used (2–3 pc versus their 0.05 pc).

Comparing the results in W49 by Barnes et al. (2020) with those of Orion B by Pety et al. (2017) further comes up with interesting differences: for Orion B, h_Q (the emission efficiency as they call it) for HCN peaks at a lower column density than for N_2H^+ , while in W49 they found the two peak points comparable, with N_2H^+ even

potentially peaking at lower column densities. To investigate this, Barnes et al. (2020) assessed how h_Q varies as a function of dust temperature and column density simultaneously. They found that the majority of the line emission of HCN is towards moderate-high temperatures (around 30–35 K), while for N_2H^+ it is at around the lowest observed temperatures at the highest column density within the observed parameter space (around 20 K). There is also another peak for N_2H^+ at higher temperatures. They explain the difference with the different chemical formation pathways of the two species which can result in them favouring different temperature regimes and can have important effects on the gas that we may trace using them.

As mentioned in Section 2.5, the different ways of computing dense gas fraction for our structures will introduce varying biases regarding the behaviour of tracers in the interstellar radiation field (shielding, depletion, photodissociation, etc.) but even so, the detection of higher dense gas fraction in the interarm regions in our data seems counter-intuitive. One explanation may be the higher protostellar clump fraction in the arm regions. Newly forming stars will heat the surrounding gas and dust, which can enhance the CO emission by both desorbing frozen-out molecules and so enhancing the abundance, and due to the higher gas temperatures, enhancing the excitation temperature of the molecule (Clark et al. 2012). We would therefore expect the ^{13}CO brightness to correlate with the Hi-GAL temperature, which does occur in the arm filament regions, as mentioned. N_2H^+ is destroyed efficiently by gas-phase CO, so the enhanced CO abundance may to some extent counteract the increased excitation for this molecule, which is consistent with the observed lack of correlation between N_2H^+ brightness and temperature. Tafalla et al. (2023) recently found that the amount of CO emission per unit column density is higher in Orion A than in the Perseus and California clouds, while the N_2H^+ emission is unchanged. They attribute this to the generally higher temperatures in the actively star-forming Orion complex, which is consistent with the scenario outlined above.

The interarm clouds could also suffer from the intense photodissociation of CO since the interstellar radiation field ‘seen’ by the gas is $G_0 \times e^{-A_V}$ and the exponential term is potentially more important for the gas on the outskirts of the cloud where most of the mass is located. Inside the dense regions, the term should be a small number, thus irrelevant, explaining the missing CO. The G_0 term can also be much higher in the interarm than in the arm, since the high-mass star forming regions along the edge of the nearby arm(s) might shine into the interarm region in a less interrupted way than in the clouds inside the arm where the arm material can shield inner areas (Porter, Johannesson & Moskalenko 2017; Clark et al. 2019). The N_2H^+ brightness can also be boosted by embedded star formation. The PPMAP dust temperature maps show both the interarm and arm filament around 20 K, however the separately derived T_{dust} values for Hi-GAL clumps of Elia et al. (2021) based on their own fitting procedure show the average T_{dust} of Hi-GAL/ N_2H^+ clusters in the interarm with 15.3 K while in the arm, 20.4 K. However, we must consider the many uncertainties in deriving the large-scale dust temperature maps used in these results e.g. foreground, background, spectral index, the usage of single-temperature fits, and the probability distribution in the results of the PPMAP procedure.

Another way to explain higher ^{13}CO brightness in the arm filament is the presence of CO-bright material that is not associated with star formation, but rather forms in transient, dense shocks. These will likely get sheared apart by the very motions that create them, while in the interarm, this would happen less frequently or not at all: most

of the CO that we see is likely to be associated with bound clouds since they formed in the arm and managed to survive.

We also call attention to the assumptions used during our calculation of the optical depth, excitation temperature and column density of N_2H^+ that might introduce errors in the derived parameters e.g. optically thin conditions were assumed but as the calculations proved, the $N_2H^+(1-0)$ emission is optically thick, and a filling factor of 1 was assumed, however this might be an overestimation. Additionally, it is worth mentioning here again the results by Barnes et al. (2020) who find that the emission efficiency of N_2H^+ in W49 peaks at two locations in the $T_{dust} - N(H_2)_{dust}$ space. The stronger peak is at lower temperatures, while the emission is less efficient but significant in warmer environments. This might also influence the amount of N_2H^+ we detect in our regions in different environmental characteristics.

4.4 Extragalactic outlook

Regarding the extragalactic implications of the current study, there are only a small number of extragalactic maps analysing $N_2H^+(1-0)$ emission as of date, however, with the large surveys of ALMA and the IRAM telescopes (e.g. EMPIRE, ALCHEMI) near-future influx of new results is expected. Harada et al. (2019) studied the circumnuclear ring of M83 with ALMA and observed different $N_2H^+(1-0)/^{13}CO(1-0)$ ratios at different positions, generally between 0.1 and 0.24. They explain the variation with potentially increasing N_2H^+ abundance in a collapsing pre-stellar core (shocks compress gas and increase the dense gas fraction). Comparison with our results is difficult, however, due to the different observed ^{13}CO isotopologue and the vastly different scales involved (their ‘clumps’ are 50–100 pc large, thus, around a hundred times larger than ours). Their N_2H^+ column densities are in line with the higher values we measure (a few times 10^{12} – 10^{13} cm^{-2}) and their excitation temperatures are around 6 K, which we only measure in Region 6. Eibensteiner et al. (2022) observed 2 and 3 mm molecular lines towards the centre of NGC 6946 with the Northern Extended Millimeter Array (NOEMA), however, they do not analyse N_2H^+ separately, only against the emission of HCN.

Jiménez-Donaire et al. (2023) observed $N_2H^+(1-0)$ in the spiral galaxy NGC 6946 across different environments and found a strong correlation of its emission with HCN at kiloparsec scales. They made pointed observations of HCN and N_2H^+ and observe that although the HCN/CO ratio does decrease with galactocentric radius, N_2H^+ seems to be constant. Thus, their primary result is that there is a strong correlation of HCN and N_2H^+ through different scales and orders of magnitude. They find N_2H^+/CO values between 0.002 and 0.0047 with no significant difference between arm and interarm regions. Recently, the NOEMA mapping of M51 was published by Stuber et al. (2023) also presenting the line ratios of HCN, N_2H^+ , and ^{12}CO , this time on smaller spatial scales. Their fit to the N_2H^+ versus HCN line emissions in the central region of the galaxy close to its AGN is in better agreement with the values computed by Jiménez-Donaire et al. (2023), but differ from those when fitting values observed on pixels in the N_2H^+ -bright south-western spiral arm of M51. The investigation of the N_2H^+ -to-HCN ratio in our filaments will be the topic of a future paper.

5 CONCLUSIONS

We performed large-scale on-the-fly mapping of dense gas tracers along two giant molecular filaments in the Galaxy, one associated with the Sagittarius arm and one with an interarm environment. We used the $N_2H^+(1-0)$ transition to trace the dense gas and compare

its distribution to tracers of more extended and diffuse gas, namely $^{13}\text{CO}(3-2)$ and dust emission. The ratio of dense to diffuse gas over a fixed area, what we call the dense gas fraction and measure with two parameters, f'_{DG} and $h_{\text{N}_2\text{H}^+}$, may be a key indicator of star formation efficiency, thus investigating their environmental differences is of utmost importance.

Our main findings are:

(i) The $\text{N}_2\text{H}^+(1-0)$ emission generally traces the brightest $^{13}\text{CO}(3-2)$ -emitting and dusty features of the filaments with a filling factor of around 8.5 per cent. This dense gas appears in small, roughly parsec-sized clusters with no substructure on the observed scales.

(ii) Evaluating the correlation of the $^{13}\text{CO}(3-2)$ and $\text{N}_2\text{H}^+(1-0)$ emission and their ratio, f'_{DG} , an analogous expression to the dense gas mass fraction, interarm cloud regions show a larger fraction of dense gas on average than the Sagittarius-arm filament. This is also observable by calculating the average f'_{DG} of the individual N_2H^+ clusters extracted with dendrogram clustering, resulting in values of 0.60 for the interarm filament and 0.31 for the arm filament.

(iii) Another dense gas mass fraction-analogous value, $h_{\text{N}_2\text{H}^+}$, is observed to be less changeable but still showing variations between the two filaments based on the cluster-averaged values, with $2.0 \text{ K km s}^{-1}/10^{22} \text{ cm}^{-2}$ for the interarm and $1.41 \text{ K km s}^{-1}/10^{22} \text{ cm}^{-2}$ for the arm filament.

(iv) The arm filament is generally seen brighter in $^{13}\text{CO}(3-2)$ and dust IR emission than the interarm cloud. There is, however, no such significant difference in their $\text{N}_2\text{H}^+(1-0)$ emission. There also exists a $N(\text{H}_2)_{\text{dust}}$ threshold above which $\text{N}_2\text{H}^+(1-0)$ emission starts appearing in the mapped areas. This threshold value is observed to be higher for the arm filament.

(v) N_2H^+ clusters in the arm filament are seen as more evolved since all of them are associated with clumps in the protostellar phase, while interarm clusters appear as both protostellar and pre-stellar/starless. We do not see a significant difference between the average dust temperatures in the arm and interarm on large scales, but the arm N_2H^+ clusters seem somewhat warmer.

(vi) Scenarios involving enhanced CO abundance in higher temperature gas, the observed molecular clouds suffering from the photodissociation by the ISRF at differing levels depending on their Galactic location, the appearance of less and more unbound, transient CO-clouds, or peculiarities in the emission efficiency of N_2H^+ can explain the observed discrepancy of dense gas fraction between the arm and the interarm.

ACKNOWLEDGEMENTS

OF, SER, FDP, and PCC acknowledge the support of a consolidated grant (ST/K00926/1) from the UK Science and Technology Facilities Council (STFC). This work is based on observations carried out under project number 033-17 and E02-22 with the IRAM 30m telescope. IRAM was supported by INSU,CNRS (France), MPG (Germany), and IGN (Spain). The James Clerk Maxwell Telescope has historically been operated by the Joint Astronomy Centre on behalf of the Science and Technology Facilities Council of the United Kingdom, the National Research Council of Canada, and the Netherlands Organisation for Scientific Research. This research made use of Astropy (Astropy Collaboration 2022, <https://astropy.org>), a community-developed core Python package for Astronomy as well as the Python packages NUMPY (Oliphant et al. 2006, <https://numpy.org>), SCIPY (Virtanen et al. 2020, <https://scipy.org>), MATPLOTLIB (Hunter 2007, <https://matplotlib.org>), and astrodendro (<http://www.dendrograms.org>). This publication has also made use SAOImageDS9 (Joye &

Mandel 2003, <http://ds9.si.edu>), an astronomical imaging and data-visualization application and the CLASS and GREG software packages of GILDAS (<https://www.iram.fr/IRAMFR/GILDAS>). This research used the Canadian Advanced Network For Astronomy Research (CANFAR) operated in partnership by the Canadian Astronomy Data Centre and The Digital Research Alliance of Canada with support from the National Research Council of Canada the Canadian Space Agency, CANARIE and the Canadian Foundation for Innovation.

DATA AVAILABILITY

The data underlying this article will be shared on reasonable request to the corresponding author.

REFERENCES

- Abreu-Vicente J., Ragan S., Kainulainen J., Henning T., Beuther H., Johnston K., 2016, *A&A*, 590, A131
- Aguirre J. E. et al., 2011, *ApJS*, 192, 4
- Aladro R. et al., 2015, *A&A*, 579, A101
- André P., Belloche A., Motte F., Peretto N., 2007, *A&A*, 472, 519
- Astropy Collaboration, 2022, *ApJ*, 935, 167
- Barnes A. T. et al., 2020, *MNRAS*, 497, 1972
- Battersby C., Bally J., 2014, in *The Labyrinth of Star Formation*, Vol. 36, Astrophysics and Space Science Proceedings. Springer-Verlag, Berlin, p. 417
- Battisti A. J., Heyer M. H., 2014, *ApJ*, 780, 173
- Benson P. J., Caselli P., Myers P. C., Goodman A. A., 1994, in Clemens D. P., Barvainis R. eds, *ASP Conf. Ser.*, Vol. 65, *Clouds, Cores, and Low Mass Stars*. Astron. Soc. Pac., San Francisco, p. 67
- Bigiel F., Leroy A., Walter F., Brinks E., de Blok W. J. G., Madore B., Thornley M. D., 2008, *AJ*, 136, 2846
- Bigiel F. et al., 2016, *ApJ*, 822, L26
- Caselli P., Myers P. C., Thaddeus P., 1995, *ApJ*, 455, L77
- Clark P. C., Glover S. C. O., Klessen R. S., Bonnell I. A., 2012, *MNRAS*, 424, 2599
- Clark P. C., Glover S. C. O., Ragan S. E., Duarte-Cabral A., 2019, *MNRAS*, 486, 4622
- Cordes J., in Clemens D., Shah R., Brainerd T., eds, 2004, *ASP Conf. Ser.*, Vol. 217, *Milky Way Surveys: The Structure and Evolution of our Galaxy*. Astron. Soc. Pac., San Francisco, p. 317
- Dame T. M., Hartmann D., Thaddeus P., 2001, *ApJ*, 547, 792
- Dempsey J. T., Thomas H. S., Currie M. J., 2013, *ApJS*, 209, 8
- Eden D. J., Moore T. J. T., Morgan L. K., Thompson M. A., Urquhart J. S., 2013, *MNRAS*, 431, 1587
- Eibensteiner C. et al., 2022, *A&A*, 659, A173
- Elia D. et al., 2021, *MNRAS*, 504, 2742
- Fernández-López M. et al., 2014, *ApJ*, 790, L19
- Forbrich J., Öberg K., Lada C. J., Lombardi M., Hacar A., Alves J., Rathborne J. M., 2014, *A&A*, 568, A27
- Friesen R. K., Bourke T. L., Di Francesco J., Gutermuth R., Myers P. C., 2016, *ApJ*, 833, 204
- Gao Y., Solomon P. M., 2004, *ApJ*, 606, 271
- Glover S. C. O., Mac Low M. M., 2011, *EAS Publ. Ser.*, 52, 147
- Goodman A. A. et al., 2014, *ApJ*, 797, 53
- Harada N., Sakamoto K., Martín S., Watanabe Y., Aladro R., Riquelme D., Hirota A., 2019, *ApJ*, 884, 100
- Hildebrand R. H., 1983, *Q. J. R. Astron. Soc.*, 24, 267
- Hunter J. D., 2007, *Comput. Sci. Eng.*, 9, 90
- Jackson J. M. et al., 2006, *ApJS*, 163, 145
- Jiménez-Donaire M. J. et al., 2023, *A&A*, 676, L11
- Johnston K. G., Shepherd D. S., Aguirre J. E., Dunham M. K., Rosolowsky E., Wood K., 2009, *ApJ*, 707, 283
- Jones G. H., Clark P. C., Glover S. C. O., Hacar A., 2023, *MNRAS*, 520, 1005

Joye W. A., Mandel E., 2003, in Payne H. E., Jedrzejewski R. I., Hook R. N., eds, ASP Conf. Ser., Vol. 295, Astronomical Data Analysis Software and Systems XII. Astron. Soc. Pac., San Francisco, p. 489

Juvela M. et al., 2012, *A&A*, 541, A12

Juvela M. et al., 2015, *A&A*, 584, A93

Kainulainen J., Beuther H., Henning T., Plume R., 2009, *A&A*, 508, L35

Kainulainen J., Ragan S. E., Henning T., Stutz A., 2013, *A&A*, 557, A120

Kauffmann J., Goldsmith P. F., Melnick G., Tolls V., Guzman A., Menten K. M., 2017, *A&A*, 605, L5

Kennicutt R. C. J., 1998, *ApJ*, 498, 541

Keown J. et al., 2017, *ApJ*, 850, 3

Lada C. J., Lombardi M., Alves J. F., 2010, *ApJ*, 724, 687

Lada C. J., Forbrich J., Lombardi M., Alves J. F., 2012, *ApJ*, 745, 190

Lee Y., Stark A. A., Kim H.-G., Moon D.-S., 2001, *ApJS*, 136, 137

Mangum J. G., Shirley Y. L., 2015, *PASP*, 127, 266

Marsh K. A., Whitworth A. P., Lomax O., 2015, *MNRAS*, 454, 4282

Marsh K. A. et al., 2017, *MNRAS*, 471, 2730

Martín S. et al., 2021, *A&A*, 656, A46

Mauersberger R., Henkel C., 1991, *A&A*, 245, 457

Milam S. N., Savage C., Brewster M. A., Ziurys L. M., Wyckoff S., 2005, *ApJ*, 634, 1126

Moore T. J. T., Urquhart J. S., Morgan L. K., Thompson M. A., 2012, *MNRAS*, 426, 701

Nishimura Y., Shimonishi T., Watanabe Y., Sakai N., Aikawa Y., Kawamura A., Yamamoto S., 2016, *ApJ*, 818, 161

Oliphant J., White D., Bolton M., Maconochie A., Bonab M., 2006, Proceedings of the Deep Offshore Technology Conference, Vol. 1, Models Tests Stimulating Catenary Riser-Soil Interaction. DOTC, Houston, USA, p. 1

Pety J. et al., 2017, *A&A*, 599, A98

Porter T., Johannesson G., Moskalenko I., 2017, Proc. Sci. 35th International Cosmic Ray Conference - PoS (ICRC2017). SISSA, Trieste, #737

Priestley F. D., Clark P. C., Glover S. C. O., Ragan S. E., Fehér O., Prole L. R., Klessen R. S., 2023a, *MNRAS*, 526, 4952

Priestley F. D., Clark P. C., Glover S. C. O., Ragan S. E., Fehér O., Prole L. R., Klessen R. S., 2023b, *MNRAS*, 524, 5971

Purcell C. R., Longmore S. N., Burton M. G., Walsh A. J., Minier V., Cunningham M. R., Balasubramanyam R., 2009, *MNRAS*, 394, 323

Qi C., Öberg K. I., Wilner D. J., 2013, *ApJ*, 765, 34

Ragan S. E., Henning T., Tackenberg J., Beuther H., Johnston K. G., Kainulainen J., Linz H., 2014, *A&A*, 568, A73

Ragan S. E., Moore T. J. T., Eden D. J., Hoare M. G., Elia D., Molinari S., 2016, *MNRAS*, 462, 3123

Rigby A. J. et al., 2016, *MNRAS*, 456, 2885

Rosolowsky E. W., Pineda J. E., Kauffmann J., Goodman A. A., 2008, *ApJ*, 679, 1338

Ruze J., 1966, *Proc. IEEE*, 54, 633

Schinnerer E. et al., 2017, *ApJ*, 836, 62

Schmidt M., 1959, *ApJ*, 129, 243

Schöier F. L., van der Tak F. F. S., van Dishoeck E. F., Black J. H., 2005, *A&A*, 432, 369

Shetty R., Kelly B. C., Rahman N., Bigiel F., Bolatto A. D., Clark P. C., Klessen R. S., Konstantin L. K., 2014, *MNRAS*, 437, L61

Shirley Y. L., 2015a, *PASP*, 127, 299

Shirley Y. L., 2015b, *PASP*, 127, 299

Shirley Y. L. et al., 2013, *ApJS*, 209, 2

Smith R. J., Glover S. C. O., Clark P. C., Klessen R. S., Springel V., 2014, *MNRAS*, 441, 1628

Stark A. A., Lee Y., 2006, *ApJ*, 641, L113

Stephens I. W., Jackson J. M., Whitaker J. S., Contreras Y., Guzmán A. E., Sanhueza P., Foster J. B., Rathborne J. M., 2016, *ApJ*, 824, 29

Stuber S. K. et al., 2023, *A&A*, 680, L20

Sun J. et al., 2018, *ApJ*, 860, 172

Tafalla M., Usero A., Hacar A., 2023, *A&A*, 679, A112

Taylor J. H., Cordes J. M., 1993, *ApJ*, 411, 674

Turner B. E., Thaddeus P., 1977, *ApJ*, 211, 755

Virtanen P. et al., 2020, *Nat. Methods*, 17, 261

Wang K., Testi L., Ginsburg A., Walmsley C. M., Molinari S., Schisano E., 2015, *MNRAS*, 450, 4043

Wang K., Testi L., Burkert A., Walmsley C. M., Beuther H., Henning T., 2016, *ApJS*, 226, 9

Watanabe Y., Sakai N., Sorai K., Yamamoto S., 2014, *ApJ*, 788, 4

Wienen M., Wyrowski F., Schuller F., Menten K. M., Walmsley C. M., Bronfman L., Motte F., 2012, *A&A*, 544, A146

Wolfire M. G., Hollenbach D., McKee C. F., 2010, *ApJ*, 716, 1191

Wu J., Evans Neal J. I., Shirley Y. L., Knez C., 2010, *ApJS*, 188, 313

Yu N.-P., Xu J.-L., Wang J.-J., Liu X.-L., 2018, *ApJ*, 865, 135

Zucker C., Battersby C., Goodman A., 2015, *ApJ*, 815, 23

Zucker C., Battersby C., Goodman A., 2018, *ApJ*, 864, 153

APPENDIX A: DERIVING PHYSICAL PARAMETERS FROM THE N_2H^+ SPECTRA

Following the method used by Purcell et al. (2009), we derived the full optical depth of the transition in a pixel-by-pixel manner using the HF components of $N_2H^+(1-0)$ line. We perform the calculations only on pixels where the S/N of both group 2 and group 1 was higher than 3. We note here that as described before, the weakest group 1 of the $N_2H^+(1-0)$ HFS was often not detected which influences our ability to calculate $\tau_{N_2H^+}$. Thus, occasionally, even when the main group of the transition was detected with a high S/N, we do not have a good estimation of the optical depth and the N_2H^+ column density (e.g. towards the fairly bright cluster R6CL7).

Assuming optically thin conditions and that the linewidths and the excitation temperatures of the individual HF components are equal, the integrated intensities of the three groups that the seven HF components blend into should be in the ratio of 1:5:2. The optical depth is calculated from the integrated intensities of any two groups using:

$$\frac{\int T_{MB,1} dv}{\int T_{MB,2} dv} = \frac{1 - e^{-\tau_1}}{1 - e^{-a\tau_1}}, \quad (A1)$$

where a is the expected ratio of the optical depths of the two groups, τ_1 and τ_2 . Since Caselli, Myers & Thaddeus (1995) reports anomalous excitation of HF components in group 3 (at the lowest frequencies), we determine the optical depth from the intensity ratio of group 1 and 2.

The general equation to calculate molecular column densities from Mangum & Shirley (2015) is:

$$N(\text{total}) = \frac{3h}{8\pi^3 |\mu_{lu}|^2} \frac{Q_{\text{rot}}}{g_u} \exp\left(\frac{E_u}{kT_{\text{ex}}}\right) \times \left[\exp\left(\frac{hv}{kT_{\text{ex}}} - 1\right) \right]^{-1} \int \tau_\nu dv, \quad (A2)$$

where Q_{rot} is the rotational partition function, g_u is the degeneracy of the energy level u , μ_{lu} is the dipole matrix element, E_u is the energy of level u , ν is the frequency of the transition, h is the Planck constant, and k is the Boltzmann constant. In the case of $N_2H^+(1-0)$, assuming optically thin emission and an approximation to the integrated optical depth expression, this leads to:

$$N(N_2H^+) = 1.20 \times 10^{12} (T_{\text{ex}} + 0.75) \frac{\exp\left(\frac{4.47}{T_{\text{ex}}}\right)}{\exp\left(\frac{4.47}{T_{\text{ex}}}\right) - 1} \times \frac{\tau}{1 - \exp(-\tau)} \left[\frac{\int T_{MB} dv (\text{km/s})}{f (J_\nu(T_{\text{ex}}) - J_\nu(T_{\text{bg}}))} \right] \text{cm}^{-2}, \quad (A3)$$

where f is the beam filling fraction, T_{bg} is the background temperature 2.7 K, $(T_{\text{ex}} + 0.75)$ is an approximation of the partition

function and

$$J_\nu(T) = \frac{\left(\frac{h\nu}{k}\right)}{\left(\exp\left(\frac{h\nu}{kT}\right) - 1\right)}. \quad (\text{A4})$$

In general, T_{ex} varies between the background radiation temperature at low densities and T_{kin} gas kinetic temperature at high density. A transition is said to be thermalized if $T_{\text{ex}} = T_{\text{kin}}$. In the general case of non-local thermodynamic equilibrium (non-LTE) in the interstellar medium, most transitions of dense gas tracers are assumed to be subthermally populated. If the line is known to be very optically thick, the radiative transfer equation can be used to calculate excitation temperature analytically (because the $(1-e^{-\tau})$ term will approach 1). In the optically thin case, the observed line temperature is degenerate with $T_{\text{ex},\tau}$, and the filling fraction and we need to use multiple transitions using a rotation diagram. In the case

of our $\text{N}_2\text{H}^+(1-0)$ data (dense gas, assuming LTE, probably not very optically thick medium) we use the results obtained in CLASS by fitting the HFS.

The derived excitation temperatures are lowest in Region 2 with 3.1 K and highest in Region 3 with 4.3 K. The $\tau_{\text{N}_2\text{H}^+}$ optical depth is measured overwhelmingly above 1 (i.e. optically thick radiation) with the highest values in Region 2 with 10 and the lowest in Region 3 and Region 5 with 3.1 and 3.9. Finally, N_2H^+ column densities are generally between $0.2\text{--}0.5 \times 10^{14} \text{ cm}^{-2}$ except in Region 2 where it is higher with $1.2 \times 10^{14} \text{ cm}^{-2}$. The average $T_{\text{ex},\tau}$ and $N(\text{N}_2\text{H}^+)$ for the N_2H^+ clusters can be found in Table B1 wherever the observed spectra was detected with a good enough S/N to compute those.

APPENDIX B: FIGURES AND TABLES

Table B1. The parameters of the N_2H^+ clusters identified with the dendrogram method. (1) The identifier of the cluster; (2,3) equatorial coordinates; (4,5) major and minor axis length; (6) position angle from the equator in clockwise direction; (7,8) average velocity and HF linewidth; (9) average optical depth; (10) average N_2H^+ column density; (11, 12) average ^{13}CO and N_2H^+ integrated intensity; (13) average H_2 column density from dust emission. Missing values could not be computed due to insufficient S/N on the location of the cluster. The symbol * marks clusters where only a single value of a parameter was available (thus it is not an average).

ID	RA ($^\circ$)	DEC ($^\circ$)	a (arcsec)	b (arcsec)	PA ($^\circ$)	v_{LSR} (km s^{-1})	Δv_{HFS} (km s^{-1})	τ	$N(\text{N}_2\text{H}^+)$ (10^{14} cm^{-2})	$W(^{13}\text{CO})$ (K km s^{-1})	$W(\text{N}_2\text{H}^+)$ (K km s^{-1})	$N(\text{H}_2)_{\text{dust}}$ (10^{22} cm^{-2})
R1CL1	284.60697	3.03848	49.1	20.7	-143	75.9 (0.2)	1.77 (0.16)	2.0 (0.8)	0.27 (0.07)	15.4 (3.1)	4.5 (0.9)	2.00 (0.30)
R1CL2	284.63488	3.04875	18.0	13.3	167	80.8* (0.0)	-	-	-	16.3 (2.8)	2.6 (0.3)	1.61 (0.06)
R1CL3	284.59294	3.07755	24.5	17.1	60	75.0 (0.1)	1.25 (0.30)	9.12 (1.4)	0.48 (0.07)	6.2 (1.0)	1.8 (0.2)	1.27 (0.03)
R1CL4	284.61032	3.00986	17.4	13.1	105	79.5 (0.1)	1.05 (0.0)	8.32*	0.46*	3.9 (0.7)	1.8 (0.3)	1.34 (0.02)
R1CL5	284.59118	3.02467	19.8	17.8	146	88.6* (0.0)	-	-	-	3.4 (0.7)	2.5 (0.4)	1.72 (0.06)
R1CL6	284.59325	3.04520	39.0	20.9	88	77.7 (1.6)	1.26 (0.24)	3.81 (2.7)	0.33 (0.19)	4.4 (1.8)	2.5 (0.4)	1.71 (0.10)
R1CL7	284.60066	3.09832	23.6	17.2	117	52.5 (0.2)	1.05 (0.0)	5.58 (2.8)	0.50 (0.15)	2.3 (0.8)	1.7 (0.2)	1.54 (0.07)
R2CL1	284.76666	3.42842	15.9	13.4	123	78.5 (0.3)	1.05 (0.00)	-	-	15.2 (0.7)	2.8 (0.4)	1.68 (0.12)
R2CL2	284.76436	3.44348	21.5	18.5	117	83.9 (0.0)	-	-	-	5.3 (1.7)	4.1 (2.2)	1.24 (0.04)
R2CL3	284.80803	3.34650	22.8	19.8	67	77.2 (0.1)	1.37 (0.15)	-	-	7.1 (1.5)	1.3 (1.5)	1.95 (0.17)
R2CL4	284.81486	3.34983	15.9	6.9	-159	-	-	-	-	5.2 (0.0)	3.2 (1.7)	1.55 (0.07)
R3CL1	284.76949	3.89697	56.7	40.1	178	91.0 (1.2)	2.11 (0.13)	1.3 (0.5)	0.30 (0.11)	13.1 (5.7)	12.4 (5.0)	3.72 (3.00)
R3CL2	284.71041	3.81477	68.6	29.1	123	89.9 (1.1)	1.70 (0.47)	2.8 (1.8)	0.20 (0.06)	3.4 (1.5)	4.8 (2.1)	1.33 (0.12)
R3CL3	284.71874	3.97830	33.3	17.8	78	92.1 (0.1)	1.26 (0.13)	3.0 (0.9)	0.18 (0.05)	8.9 (1.8)	1.8 (0.7)	1.85 (0.47)
R3CL4	284.78565	3.94774	27.9	18.8	-162	90.4 (0.1)	2.00 (0.23)	1.7 (0.4)	0.15 (0.01)	11.3 (3.5)	5.2 (0.7)	2.15 (0.56)
R3CL5	284.60774	3.78785	27.8	23.5	90	81.5 (0.1)	1.23 (0.19)	3.0 (0.9)	0.21 (0.06)	8.3 (3.6)	3.3 (1.0)	1.23 (0.11)
R4CL1	284.78465	4.26570	19.1	12.0	129	95.1* (-)	1.05*	4.6*	0.24*	5.1 (1.5)	3.2 (0.6)	1.41 (0.03)
R4CL2	284.79428	4.20338	73.8	43.8	158	84.1 (0.3)	2.45 (0.37)	2.0 (0.9)	0.21 (0.06)	12.2 (7.7)	12.0 (3.7)	3.80 (4.10)
R4CL3	284.89847	4.28015	28.5	14.8	95	86.7 (0.1)	2.05 (0.26)	8.2 (2.0)	0.29 (0.02)	17.6 (4.6)	2.4 (0.6)	2.84 (0.28)
R4CL4	284.03724	4.26913	24.3	13.9	160	86.3 (0.1)	1.76 (0.18)	5.4 (0.9)	0.19 (0.03)	3.0 (1.0)	3.3 (0.4)	1.26 (0.03)
R4CL5	284.79507	4.27264	29.6	13.7	167	86.3 (0.3)	1.19 (0.20)	5.9 (0.7)	0.21 (0.01)	2.3 (2.3)	3.4 (0.8)	1.47 (0.02)
R4CL6	284.91742	4.24616	58.6	25.4	118	82.9 (0.3)	1.52 (0.33)	5.6 (3.0)	0.19 (0.08)	4.1 (2.2)	3.7 (0.8)	1.72 (0.12)
R4CL7	284.91916	4.29636	67.7	29.1	86	88.8 (2.7)	1.64 (0.08)	4.1*	0.14*	3.1 (2.7)	2.4 (1.3)	1.35 (0.07)
R4CL8	284.83787	4.18411	25.2	19.6	116	40.8 (0.1)	1.25 (0.10)	2.3 (1.0)	0.27 (0.11)	4.0 (1.8)	1.5 (0.2)	1.67 (0.13)
R5CL1	285.02672	3.99503	44.1	21.6	52	56.9 (2.4)	1.83 (0.21)	2.2 (1.1)	0.19 (0.03)	23.2 (6.2)	5.4 (1.0)	2.61 (0.60)
R5CL2	284.93555	3.84254	14.6	9.0	125	58.1 (0.2)	...	5.6 (1.8)	0.18 (0.06)	14.3 (1.1)	1.3 (0.1)	2.13 (0.26)
R5CL3	284.96399	3.92188	16.7	10.6	176	56.6* (0.0)	2.43* (0.75)	3.9 (0.1)	0.18 (0.03)	16.7 (0.3)	4.3 (0.5)	2.26 (0.35)
R5CL4	284.92858	3.89726	48.9	20.8	76	54.6 (0.3)	1.79 (0.12)	2.2 (1.0)	0.22 (0.05)	22.1 (9.4)	5.5 (2.5)	3.27 (0.99)
R5CL5	284.97721	3.99902	19.0	12.9	-138	55.9 (0.2)	1.84*	18.2*	0.62*	19.6 (3.1)	3.0 (0.5)	2.09 (0.16)
R5CL6	285.06609	4.05690	29.8	19.7	143	50.8 (0.2)	2.27 (0.30)	2.0 (0.8)	0.16 (0.04)	39.1 (11.4)	6.3 (1.1)	4.49 (1.45)
R5CL7	285.07437	4.16839	14.7	9.7	177	50.7 (3.7)	1.34*	6.0*	0.23*	8.2 (0.0)	1.7 (0.5)	2.25 (0.10)
R5CL8	285.15250	4.22302	47.2	31.0	165	45.3 (0.4)	2.90 (0.27)	1.0 (0.5)	0.22 (0.05)	25.6 (13.3)	14.4 (3.8)	7.49 (5.37)
R5CL9	285.09970	4.13984	16.2	10.6	131	45.6 (0.1)	1.64 (0.06)	3.9 (0.5)	0.16 (0.03)	24.5 (2.0)	2.7 (0.5)	2.44 (0.18)
R6CL1	285.25712	4.20239	54.6	38.9	157	63.7 (1.8)	3.72 (0.25)	2.1 (1.9)	0.48 (0.20)	31.6 (7.9)	19.1 (5.5)	5.53 (2.72)
R6CL2	285.43692	4.26914	20.0	17.3	76	-	-	-	-	24.0 (6.5)	3.9 (0.9)	4.43 (1.58)
R6CL3	285.41506	4.16357	25.1	21.0	-166	66.0 (1.9)	2.35 (0.13)	3.0 (1.0)	0.20 (0.03)	7.3 (2.3)	6.0 (0.9)	3.93 (0.71)
R6CL4	285.43425	4.17344	35.6	24.0	106	65.4 (0.1)	2.42 (0.18)	1.8 (0.7)	0.17 (0.04)	12.9 (3.0)	6.4 (1.7)	5.32 (1.56)
R6CL5	285.23238	4.20370	34.4	20.8	134	61.2 (3.0)	2.04*	2.1*	0.20*	16.8 (6.5)	6.5 (1.5)	4.76 (2.05)
R6CL6	285.48441	4.25207	49.4	31.5	131	-	-	-	-	8.4 (4.2)	1.4 (1.5)	2.00 (0.26)
R6CL7	285.47346	4.21256	28.9	23.9	106	63.3* (0.0)	-	-	-	83.0 (21.0)	5.9 (1.3)	8.48 (4.67)

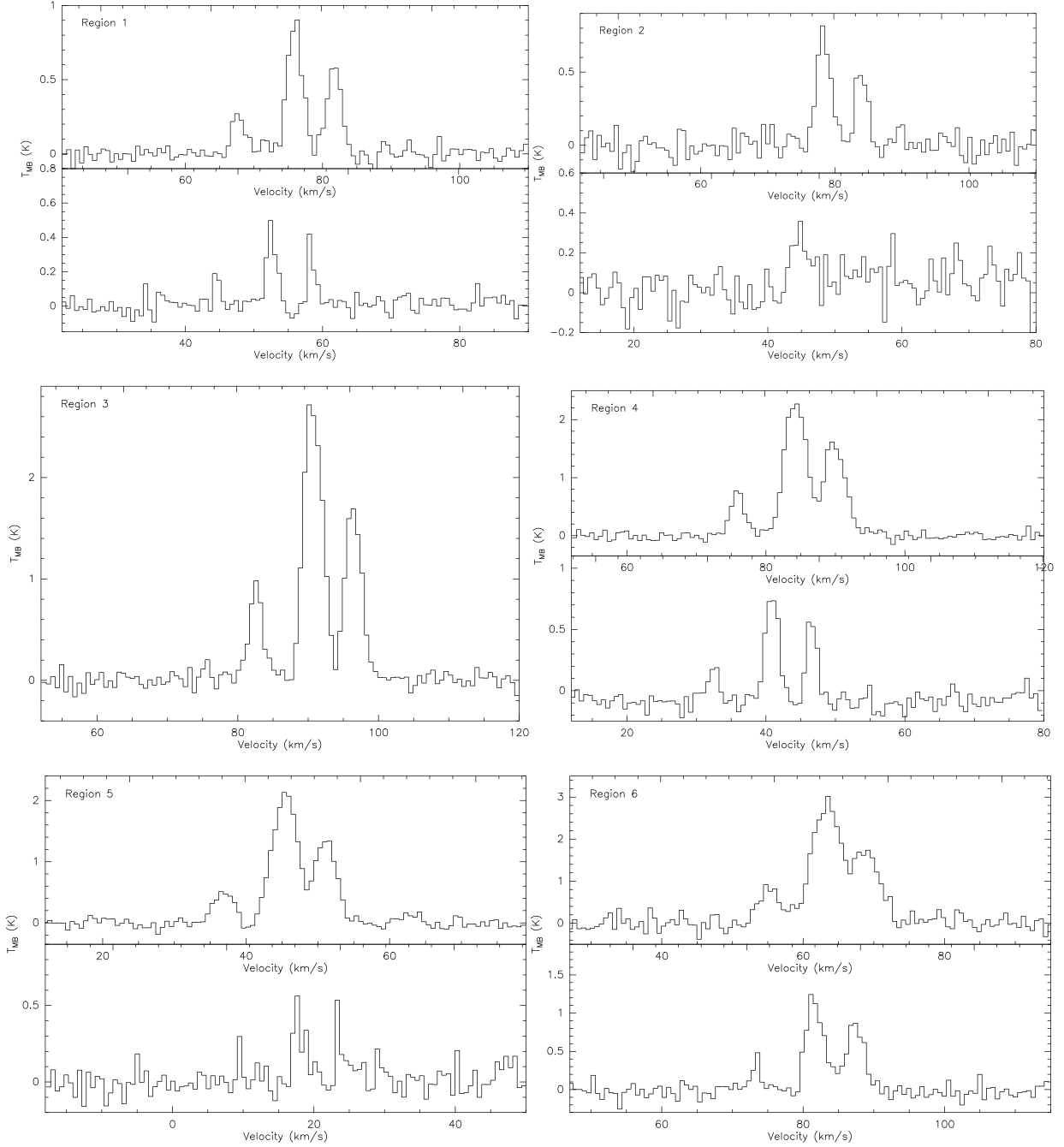


Figure B1. Average spectra showing all velocity components of $N_2H^+(1-0)$ found in the observed regions. The averaging was done centred at the integrated intensity peaks of the components and inside a single beam.

This paper has been typeset from a \LaTeX file prepared by the author.